

## The Effects of Convection on a Simulated Marine Cyclone

G. BALASUBRAMANIAN AND M. K. YAU

*Department of Atmospheric and Oceanic Sciences, McGill University, Montreal, Quebec, Canada*

(Manuscript received 11 October 1993, in final form 31 January 1994)

### ABSTRACT

A hydrostatic, primitive equation model is used to simulate an oceanic cyclone with idealized initial conditions. The model uses a pressure coordinate in the vertical with a grid spacing of 100 mb. In the horizontal a grid spacing of 25 km is used, which should be nearly sufficient to resolve slantwise convection. The model produces an explosive moist cyclone with an intense bent-back warm front. The thermal gradient in the bent-back warm frontal region exceeds 8 K/100 km, in agreement with recent observations.

Before rapid deepening, the model atmosphere becomes unstable to slantwise convection in the warm frontal region. After the spinup period, buckling in the angular momentum and  $\theta_e$  surfaces are noted. It is suggested that the descending motion and the associated dry slot over the cyclone center may arise from the descending branch of the slantwise convection on the warm side of the warm front. The descent may be augmented by the evaporation of liquid water. After the explosive deepening period, the stratification in both the warm front and the bent-back warm front exhibits neutrality to slantwise convection.

The Ertel potential vorticity (EPV) inversion technique developed by Davis and Emanuel is used to obtain the perturbation geopotential at 900-mb, 500-mb, and 300-mb levels due to EPV anomalies at different levels. The inversion is applied at the mature stage of the cyclone at 45 h. It is found that there is a positive EPV anomaly along the regions of the warm front and bent-back warm front, and it accounts for 40% of the perturbation geopotential at 900 and 500 mb over the cyclone center. The contribution of low-level EPV anomaly in the moist cyclone to the perturbation geopotential at 500 mb over the cyclone center is twice that in the dry case. The circulation of the inverted nondivergent wind fields in the moist run shows a small-scale cyclonic vortex and the presence of cold advection in the bent-back warm frontal region.

The contribution of the upper-level EPV anomaly to the 900-mb perturbation geopotential is also significant in the moist cyclone. The physical mechanism for the latter effect can be traced to an increase in vorticity advection in the middle troposphere in association with the formation of the bent-back warm front. This finding is in agreement with the authors' recent two-layer model results, which show that the bent-back warm front represents a region of cold advection that can in turn lead to an intensification of the upper-level wave. The contribution of the 1000-mb  $\theta$  anomaly in the mature moist cyclone is smaller than that of the dry run because of the convection-induced cold advection in the bent-back warm front.

### 1. Introduction

The feedback of convection and precipitation through the release of latent heat onto the dynamics of cyclogenesis has been a poorly understood area of research. Numerous investigations have examined the influence of this effect on observed cyclones (Manabe 1956; Eliassen and Kleinschmidt 1957; Danard 1964; Tracton 1973; Gyakum 1983; Liou and Elsberry 1987; Kuo and Reed 1988; Kuo et al. 1991b; Davis and Emanuel 1991, hereafter DE91; Davis et al. 1993). The results, however, indicate enormous case-to-case variability.

Motivated by observations of slantwise neutrality in the warm frontal zone of marine cyclones (Reuter and

Yau 1990, 1993), Balasubramanian and Yau (1994, hereafter BY94) investigated the physical mechanisms involved in the interaction between large-scale cyclogenesis and slantwise convection. They formulated a two-layer primitive equation model with a parameterization for slantwise convection to study explosive oceanic cyclones. The parameterization includes a simple representation of the planetary boundary layer, as well as deep and shallow cloud types. The major results are 1) the two-layer model produces a realistic explosive cyclone, 2) the explosive deepening coincides with the formation of the "bent-back warm front," 3) frontogenetic calculations reveal an indirect circulation due to the vertical "tilting" term of the frontogenetic function in the intense warm front, and 4) the quasi-Lagrangian heat and vorticity budgets indicate strong interaction of the lower- and upper-level flow during the rapid spinup stage.

These results allow BY94 to suggest a sequence of events involved in some explosive cyclogenesis. Con-

---

*Corresponding author address:* G. Balasubramanian, Dept. of Atmospheric and Oceanic Sciences, McGill University, 805 Sherbrooke Street West, Montreal, Quebec H3A 2K6, Canada.

vection leads to rapid frontogenesis and the formation of bent-back warm front. The sudden surge of cold advection in the regions of the bent-back warm front then forces the upper-level heights over the cyclone center to fall in a rather dramatic way. Increased upper-level vorticity advection interacts with the low-level system leading to explosive cyclogenesis.

While BY94 presented a qualitative picture of convective–cyclogenetical interactions, a quantitative estimate of the contribution of convection to cyclogenesis is lacking because of the crude vertical resolution in the two-layer model. To overcome this difficulty, a multilayer primitive equation model with explicit condensation has been developed. We present here a sequel to BY94 in which the structure of the simulated oceanic cyclone is described and the inversion of potential vorticity is applied to yield a quantitative picture of convective–cyclogenetical interactions.

It is recognized that to quantify accurately the contribution of convection in cyclogenesis is difficult because of nonlinear interactions. Recently, the concept of “potential vorticity (PV) thinking” (Eliassen and Kleinschmidt 1957; Hoskins et al. 1985; Thorpe 1985) has shown promise in allowing a conceptual description of the physics involved in cyclogenesis. In particular, the “invertibility principle” of PV (Hoskins et al. 1985) and the procedure of piecewise inversion of PV (Robinson 1988; DE91) have been useful in diagnosing the contribution of PV anomalies produced by individual nonconservative processes such as convection and friction to cyclogenesis. In this paper, we apply the PV diagnostics of DE91 to estimate the contribution of convection to cyclogenesis.

It is known that condensation in the low levels produces PV anomalies (Eliassen and Kleinschmidt 1957; Boyle and Bosart 1986; Whitaker et al. 1988; Kuo and Reed 1988; Hoskins and Berrisford 1988; Kuo et al. 1991a; DE91; Davis et al. 1993) of considerable magnitude. Recent observations for the ERICA IOP4 storm (Neiman and Shapiro 1993a,b) indicate that the rapid ascent and latent heat release in the bent-back warm frontal zone produce PV values as high as 6 potential vorticity units (PVU). Such a huge anomaly is expected to contribute significantly to the storm’s circulation during its mature stage. The conceptual picture of BY94 also suggests that the bent-back warm front plays an important role in the rapid spinup of some oceanic cyclones. Thus, it is natural to ask: 1) What is the nature of the circulation due to the individual PV anomaly along the bent-back warm front? 2) How does this circulation differ from that in an adiabatic cyclone? 3) How do the PV diagnostics fit into the conceptual picture proposed by BY94? We address these issues in the paper.

It should be pointed out that DE91 and Davis (1992b) have also attempted to quantify the role of condensation on cyclogenesis through PV inversion. Our study, however, differs from their work in two

fundamental aspects. First, the cases they considered, those of 15 December 1987 and 5 February 1988, are continental cyclones rather than marine cyclones. Second, they used the National Meteorological Center (NMC) global analysis data with a resolution of  $2.5^\circ$ . Interesting mesoscale structures are therefore not resolved.

In a very recent study, Davis et al. (1993) compared a continental case with two cases of marine cyclogenesis using data with a resolution of 45 km and 80 km, respectively. Their main focus is on the contribution of PV anomalies on the low-level area-averaged relative vorticity (vertical component) field. There is considerable spatial variability in the vorticity field, however, and therefore it may not be the most suitable parameter in a study of PV inversion. To alleviate this problem, we have calculated the contributions of PV anomalies to the low-level geopotential perturbation field using numerically simulated data with a resolution of 25 km.

The organization of the paper is as follows. The next section describes the model, numerical procedure, and the initial condition used in the simulation. Section 3a discusses the evolution and features of the moist cyclone, as well as its warm and bent-back warm fronts. Vertical cross sections through the warm and bent-back warm fronts are presented. Since the model has reasonable vertical resolution we analyze the stability characteristics of the atmosphere with respect to slantwise convection along the bent-back warm front. The introduction of liquid water in the model allows us to explore the role of convection in inducing the descent over the cyclone center as well. In section 3b, a brief introduction to the Ertel PV and the inversion results are discussed. We make quantitative estimates of the contribution by the PV anomalies at different levels to the geopotential perturbation at various heights over the cyclone center during the mature stage. The analysis demonstrates the effect of convection on the low, middle, and upper levels in a rather simple way. It also allows an identification of the indirect effect of enhanced upper-level influence on moist surface cyclogenesis. Finally, the concluding remarks are given in section 4.

## 2. The model

The model is an extension of the two-layer model in BY94. It solves the hydrostatic primitive equations on an  $f$  plane. New features are that the static stability can vary both horizontally and vertically, and condensation is calculated explicitly by introducing equations for water vapor and liquid water. The schematics of the model is depicted in Fig. 1.

### a. Momentum equations

The momentum equations are solved at the odd levels  $k = 1, 3, \dots, N - 1$ :

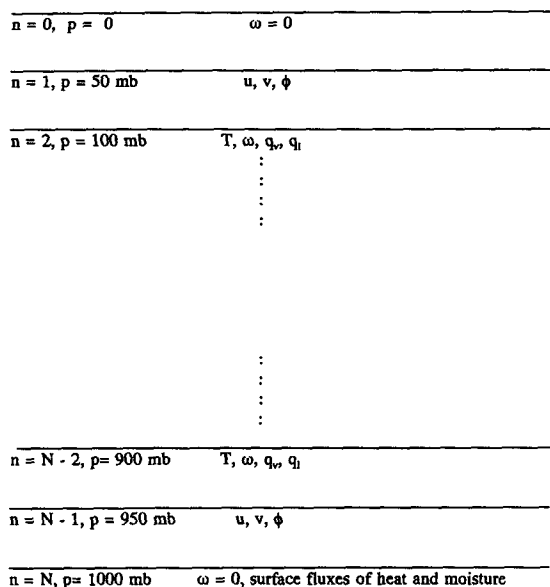


FIG. 1. The schematics of the multilayer model.

$$\frac{du_k}{dt} - fv_k = -\frac{\partial\phi_k}{\partial x} + \nu\nabla^2 u_k \quad (1)$$

$$\frac{dv_k}{dt} + fu_k = -\frac{\partial\phi_k}{\partial y} + \nu\nabla^2 v_k, \quad (2)$$

where

$$\frac{d\alpha}{dt} = \frac{\partial\alpha}{\partial t} + \frac{\partial u\alpha}{\partial x} + \frac{\partial v\alpha}{\partial y} + \frac{\partial\omega\alpha}{\partial p} \quad (3)$$

and the other symbols have their usual meteorological meanings.

#### b. Calculation of vertical velocity

The vertical velocity is assumed to vanish at both the top and bottom boundaries. The continuity equation is integrated upward to give the pressure velocities at the even levels  $k = 2, 4, \dots, N - 2$ :

$$\omega_k = \omega_{k-2} - \int_{p_{k-2}}^{p_k} (\nabla \cdot \mathbf{v}_{k-1}) dp. \quad (4)$$

#### c. Temperature equation

Since the model assumes hydrostatic equilibrium in the vertical, the thickness, defined at even levels, is directly proportional to the temperature. We solve the temperature equation at levels  $k = 2, 4, \dots, N - 2$ :

$$C_p \frac{dT}{dt} + \left( \frac{\partial\phi}{\partial p} \right)_k \omega_k = -L \left( \frac{dq_s}{dt} \right)_k + \kappa \nabla^2 T_k, \quad (5)$$

where the hydrostatic condition has been applied in deriving the second term on the left. The first term on the

right represents the heating (cooling) due to latent heat release from condensation (evaporation). At levels  $k = 2$  and  $N$ , boundary conditions discussed in section 2f would be applied.

#### d. Nonlinear balance equation

From the knowledge of temperature at level  $k$ , we can calculate the thickness  $\phi_{k-1} - \phi_{k+1}$ . We need one more equation to calculate all the  $\phi_k$ s. That is provided by the nonlinear balance equation, obtained by vertically integrating the divergence equation and requiring the mean divergence over any column to be zero. Vanishing mean divergence eliminates external gravity waves. The final form of the nonlinear equation is an elliptic equation for mean geopotential  $\phi_m = \phi_1 + \phi_3 + \dots + \phi_{N-1}$  and is given by

$$\nabla^2 \phi_m = - \sum_{k=1}^{k=N-1} \left( \frac{\partial^2 u_k^2}{\partial x^2} + 2 \frac{\partial^2 u_k v_k}{\partial x \partial y} + \frac{\partial^2 v_k^2}{\partial y^2} - f \zeta_k \right). \quad (6)$$

#### e. Moisture equations

The model treats water vapor and liquid water explicitly. The equation for water vapor mixing ratio  $q$  is

$$\frac{dq}{dt} = \left( \frac{dq_s}{dt} \right)_k + \kappa \nabla^2 q_k, \quad (7)$$

where  $q_s$  denotes the saturation mixing ratio and the first term on the right represents the source (sink) for water vapor during evaporation (condensation).

The prediction equation for liquid water mixing ratio  $l$  is

$$\frac{dl_k}{dt} = - \left( \frac{dq_s}{dt} \right)_k + \frac{\partial \Omega l_k}{\partial p} + \kappa \nabla^2 l_k, \quad (8)$$

where  $\Omega$  is the terminal fall speed of liquid water.

We consider two types of liquid water: cloud and rainwater. If the liquid water content exceeds  $1 \text{ g kg}^{-1}$ , we assume it to be rainwater; otherwise, cloud water (Takeda 1966; Rotunno and Emanuel 1987). The rainwater field is assumed to fall uniformly with a speed of  $1.2 \text{ Pa s}^{-1}$ . This speed corresponds to a terminal velocity of  $1.5 \text{ m s}^{-1}$  at lower levels and about  $3.0 \text{ m s}^{-1}$  at the 500-mb level. The cloud water is assumed to be advected by the flow. This type of simple parameterization allows us to carry one prognostic equation less but it includes the effect of precipitation downdrafts.

In the numerical procedure, the equations are first marched forward without the terms involving the phase change. Then the extra water vapor over saturation at each grid point is condensed out and latent heat released in such a way that the grid box becomes just saturated with respect to water. The condensate pro-

TABLE 1. Model parameters.

Parameter	Description	Value
$f$	Coriolis parameter	$1.0 \times 10^{-4} \text{ s}^{-1}$
$L_x$	Domain length in $x$ direction	4000 km
$L_y$	Domain length in $y$ direction	5000 km
$\Delta x = \Delta y$	Horizontal grid length	25 km
$N/2$	Number of layers in vertical	10
$\Delta p$	Vertical grid length	100 mb
$\Delta t$	Time step	45 s
$\nu = \kappa$	Diffusion coefficients	$3.5 \times 10^4 \text{ m}^2 \text{ s}^{-1}$
$C_D$	Drag coefficient	$1.0 \times 10^{-3}$

duced and associated temperature change are calculated from the following equations:

$$q_{\text{sat}}(T + \Delta T) = q(T) - \Delta q; \quad C_p \Delta T + L \Delta q = 0. \quad (9)$$

If there is subsaturation and cloud water is present, then evaporation is allowed to take place and (9) is used with the opposite sign.

#### f. Boundary conditions and boundary-layer parameterization

Periodicity is assumed in the east–west direction. We place vertical walls at  $Y = 0, L_y$ , where the normal velocity vanishes. Other conditions applied are

$$\frac{\partial u}{\partial y} = \frac{\partial T}{\partial y} = \frac{\partial q}{\partial y} = \frac{\partial l}{\partial y} = 0; \quad Y = 0, L_y. \quad (10)$$

At the top and bottom boundaries, the vertical velocity vanishes. Since the thermodynamic variables are defined at even levels, we need boundary conditions for them at  $k = 0$  and  $N$ . At the top boundary, these variables are assumed fixed in time. Since the model top is above the stratosphere and the initial condition has no water vapor or liquid water above 200 mb this condition should not exert a significant effect. At the bottom boundary,  $p = 1000$  mb, the thermodynamic variables are obtained by linear extrapolation from the 800-mb and 900-mb levels. The surface fluxes of heat and moisture are given by

$$F_\alpha = C_D |\mathbf{v}_{950}| (\alpha_s - \alpha), \quad (11)$$

where  $C_D = 1.0 \times 10^{-3}$  is the drag coefficient,  $\alpha$  represents the thermodynamic components at 950 mb, and  $\alpha_s$  is the corresponding component at the sea surface. The moisture flux is turned off when the lowest level is saturated.

#### g. Numerical details

Equation (3) shows that the advection terms are written in flux form. A staggered grid similar to the Arakawa C grid is used except that the temperature is placed at the same location as  $\omega$ . The finite-difference

equations for momentum components and temperature are space and time centered and are second-order accurate. The vapor and liquid water equations (7) and (8) are solved by the first-order accurate positive definite ‘‘upstream’’ advection scheme of Smolarkiewicz (1983).

To avoid splitting of solutions with the leapfrog scheme, a time filtering technique similar to Klemp and Wilhelmson (1978) is used for the momentum components and temperature. At the end of each time step, the nonlinear balance equation is solved using a simple overrelaxation technique. The numerical values of the parameters used in the model are listed in Table 1.

#### h. Initial conditions

The basic state of the model is obtained by specifying a zonal jet typical of midlatitude wintertime conditions and a sounding (see Table 2) at the southern boundary of the model. The temperature lapse rate is consistent with that obtained by Sanders and Gyakum (1980) from 68 ship radiosonde observations in the vicinity of rapidly deepening cyclones during the period 1971–74. The twin constraints of hydrostatic equilibrium and geostrophy are applied to obtain the temperature elsewhere in the domain. The zonal jet and the potential temperature are shown in Fig. 2a at  $X = 2000$  km. The zonal jet has a maximum velocity of  $35 \text{ m s}^{-1}$  at 200 mb with a  $1/e$  folding length of 1200 km. For simplicity we assumed that the initial relative humidity is only a function of height.

Figure 2b shows the initial fields of equivalent potential temperature  $\theta_e$  and angular momentum ( $m = u - fy$ ) at  $X = 2000$  km. The temperature and relative humidity are adjusted by trial and error to produce an initial condition that is slantwise neutral in the center of the domain and stable elsewhere.

Added to this basic state is the perturbation geopotential field and the geostrophically adjusted wind fields. Shown in Fig. 2c is the zonal cross section of the initial meridional velocity at  $Y = 2500$  km. The perturbation field has a maximum velocity of about  $6 \text{ m s}^{-1}$  at 500 mb and a vertical tilt of  $75^\circ$  between the

TABLE 2. The initial sounding at the southern boundary of the domain.

Level (mb)	Temperature (K)	Relative humidity (%)
900	290	75
800	284	85
700	278	85
600	271	80
500	263	60
400	252	40
300	238	20
200	224	0
100	224	0

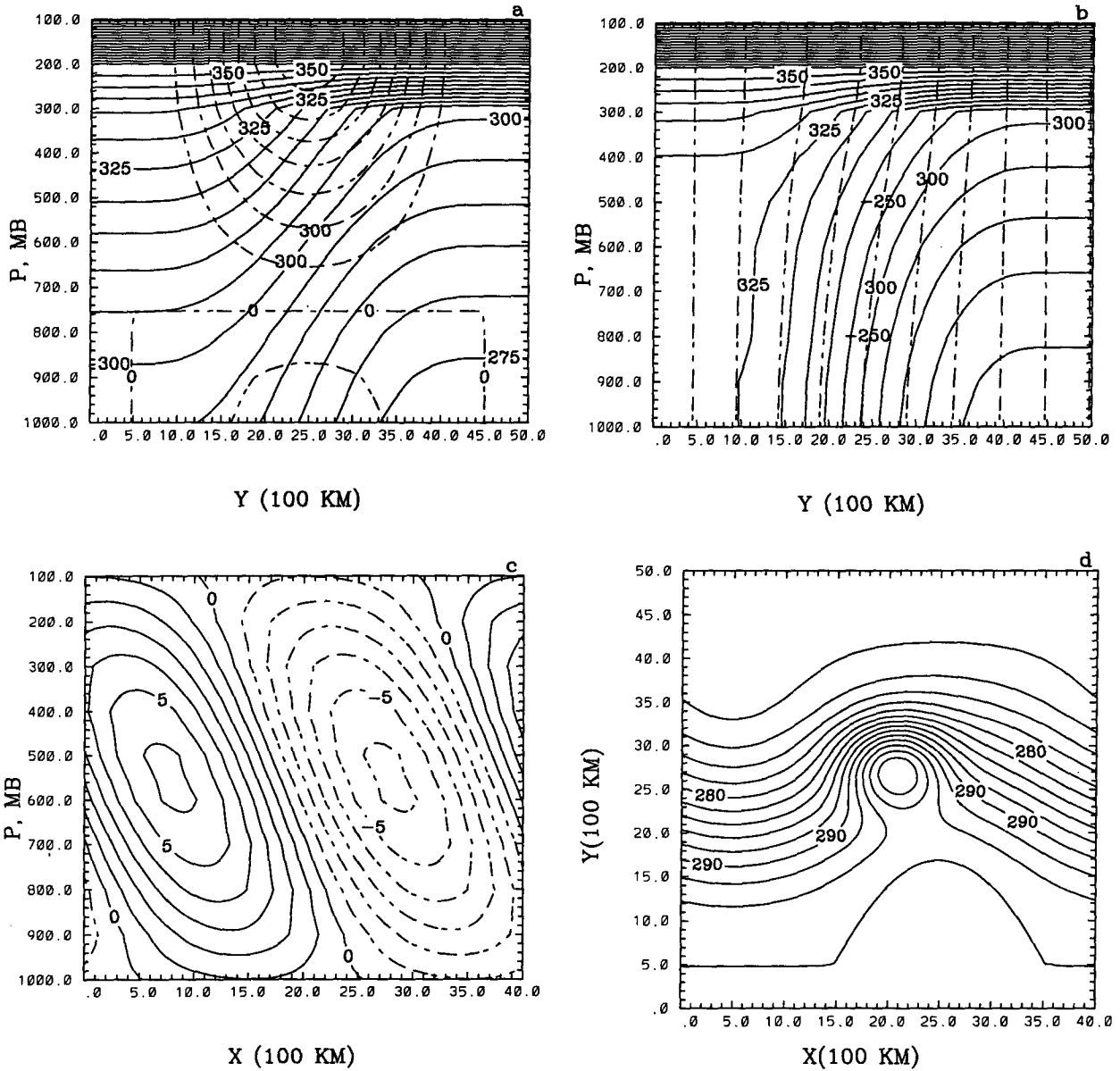


FIG. 2. The initial fields of (a) potential temperature (solid, contours every 5 K) and zonal wind (dashed, every 5 m s<sup>-1</sup>), (b) equivalent potential temperature (solid, every 5 K) and angular momentum (dashed, every 50 m s<sup>-1</sup>), (c) meridional velocity at every 1 m s<sup>-1</sup>, and (d) sea surface temperature at every 2 K.

surface and 500 mb. The sea surface temperature (Fig. 2d) consists of the temperature at 1000 mb, obtained by linear extrapolation from 800 and 900 mb, and a Gaussian perturbation of magnitude 15 K and a 1/e folding length of 500 km. The sea surface temperature is held constant during the integration.

### 3. Results

We present results mainly for an adiabatic run and a moist run. They differ only in that condensation is not allowed to take place in the adiabatic experiment. The

structure of the moist cyclone will first be described and is followed by PV diagnostics in sections 3b and 3c. For convenience, the adiabatic experiment will be referred to as the dry experiment.

#### a. Features of the moist control cyclone

Figure 3 shows the time evolution of the surface pressure drop at the center of the cyclone and the maximum of the vertical component of the 950-mb relative vorticity for both runs. The pressure deviates more or less in a steadily increasing fashion while the vorticity

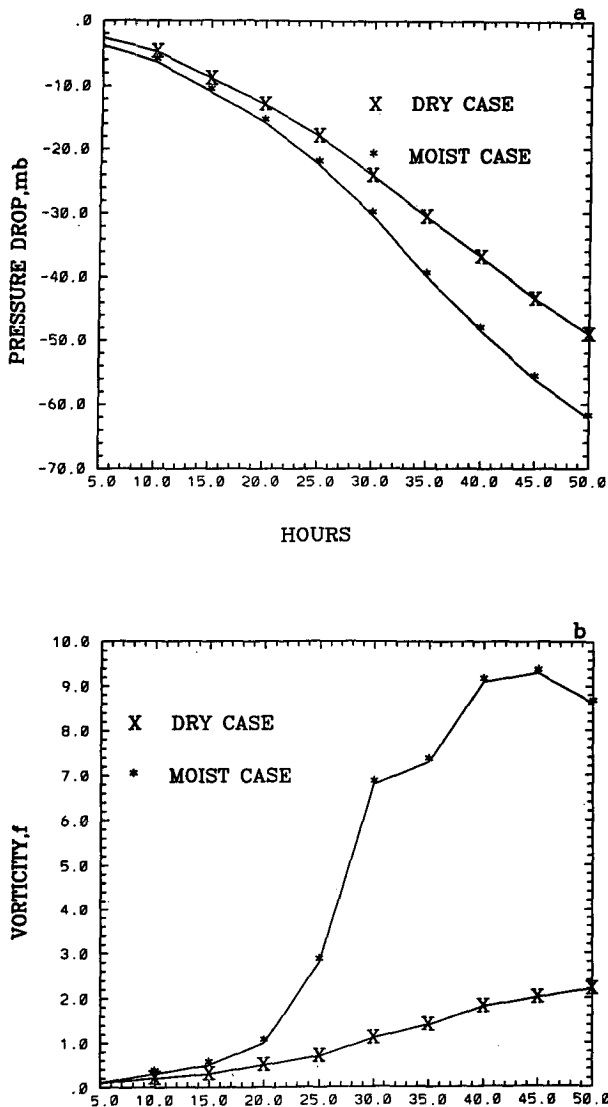


FIG. 3. Evolution of (a) surface pressure deviation and (b) maximum of the vertical component of relative vorticity at 950 mb for the moist and dry runs.

in the moist case changes in character dramatically at 20 h. At 50 h the dry and moist cyclones have pressure drops of 49 and 62 mb, respectively (Fig. 3a).

In terms of pressure drop, the dry cyclone also deepens explosively because there is strong baroclinicity in the initial conditions. However, the time series for the vertical component of the relative vorticity (Fig. 3b) indicates that the moist cyclone deviated dramatically from the dry cyclone from the early stages on. The maximum relative vorticity was located in the warm frontal region of both cyclones. While it reached a peak value of  $9.4f$  at 45 h in the moist run, the dry cyclone produced a maximum value of only  $2.2f$ . The relative vorticity field in the moist cyclone at 45 h (Fig. 4)

exhibits a crescent-shaped thin strip 250 km wide wrapping around the cyclone center. The appearance of mesoscale features within the synoptic scale is a distinct characteristic of the moist cyclone.

Figures 5 and 6 display the surface pressure deviation, the temperature, and vertical velocity at 900 mb at 25 h and 45 h, respectively. At 25 h, the isobars (Fig. 5a) show the crowding of the contours in the warm frontal zone and the cyclone center is slightly displaced toward the warm front. The sharp kinks in the isotherms are due to the sudden thermodynamic change (see the cloud edge in Fig. 7a) occurring along the sharp cloud boundary. The temperature gradient to the north of the cyclone center is about  $3\text{ K}/100\text{ km}$ . The maximum vertical velocity is located to the northeast of the cyclone center (Fig. 5b), and an organized band of large-scale ascending motion arising from convection is evident in the warm frontal zone. The organization of vertical motion in the presence of latent heat release has recently been emphasized by Fantini (1990, 1993). Since the horizontal gradients of the vertical velocity (Fig. 5b) are strong near the warm front, we can anticipate large frontogenesis due to the vertical tilting term of the frontogenetic function in this region (BY94). Note the appearance of a region of descent between the cyclone center and the warm front.

At 45 h, the cyclone enters into its mature stage (Fig. 6a). The warm front has wrapped around the cyclone center to form the bent-back warm front with a maximum thermal gradient exceeding  $8\text{ K}/100\text{ km}$ . The ascending motion has started to decay (Fig. 6b), but a narrow band of upward motion can still be noted along

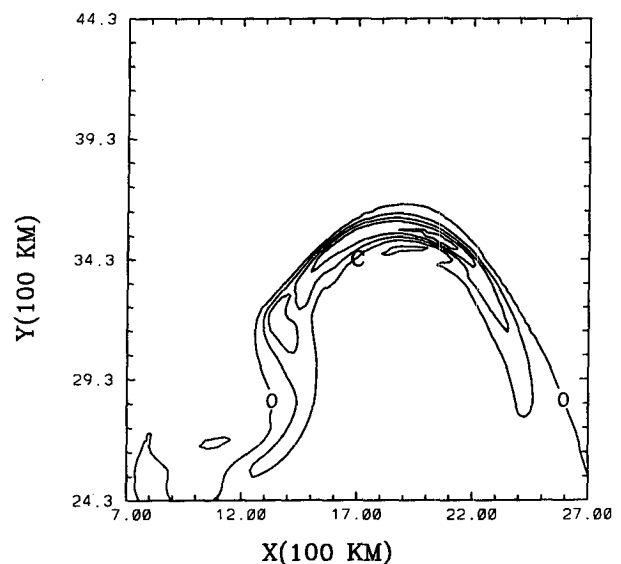


FIG. 4. Relative vorticity (vertical component) field at 950 mb at 45 h in the moist cyclone. Contour interval every  $2f$ . The label C indicates the center of the surface cyclone.

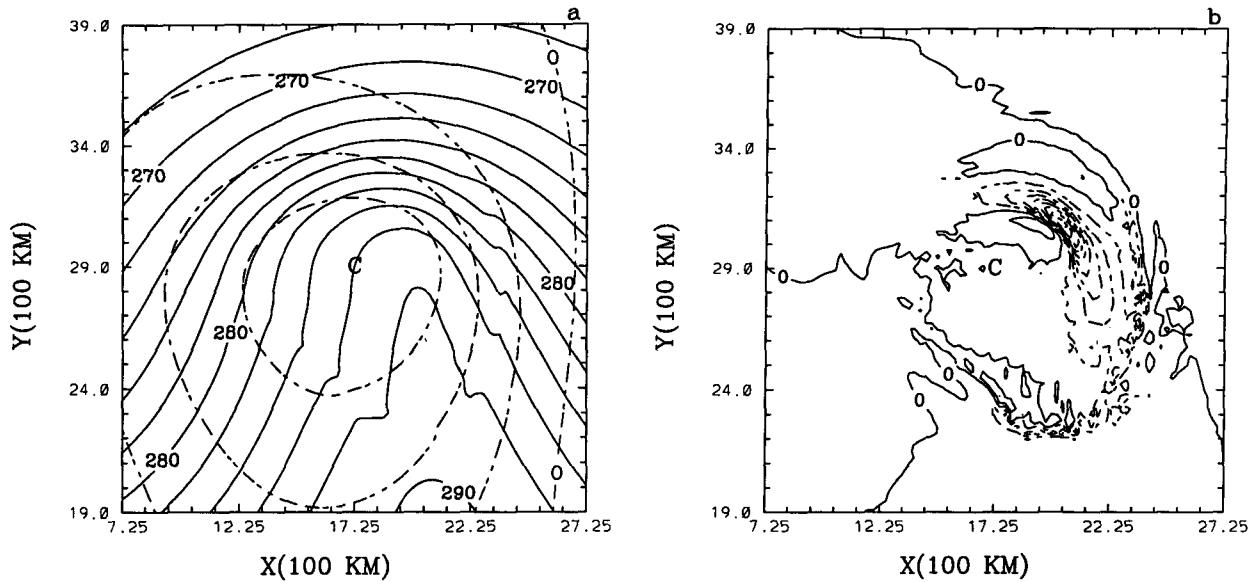


FIG. 5. The simulated fields of the moist cyclone at 25 h. (a) The surface pressure deviation (dashed, every 6 mb) and temperature at 900 mb (solid, every 2 K), and (b) pressure velocity at 900 mb (every 0.2 Pa s<sup>-1</sup>). The label C indicates the center of the surface cyclone.

the frontal region. Note that the cyclone center is located completely within a region of downward motion.

The descending motion over the center of the storm is at least partly convective in origin. To illustrate this point we plotted the 900-mb liquid water content in Fig. 7. At 25 h (Fig. 7a), the maximum in liquid water is collocated with the maximum in ascending motion. However, a local minimum in liquid water is becoming noticeable to the north of the cyclone center. This minimum expands to encompass the complete center at

35 h (Fig. 7b). A comma-shaped cloud pattern develops at 45 h (Fig. 7c) and the center of the cyclone is cloud-free.

Figure 8 depicts meridional vertical cross sections showing the angular momentum ( $m = u - fy$ ) and  $\theta_e$  surfaces. The strong potential instability to slantwise convection between the surface and 600 mb created by thermal advection and surface fluxes can be noticed at 25 h (Fig. 8a). The potential instability persists through the simulation in the unsaturated region to the south of

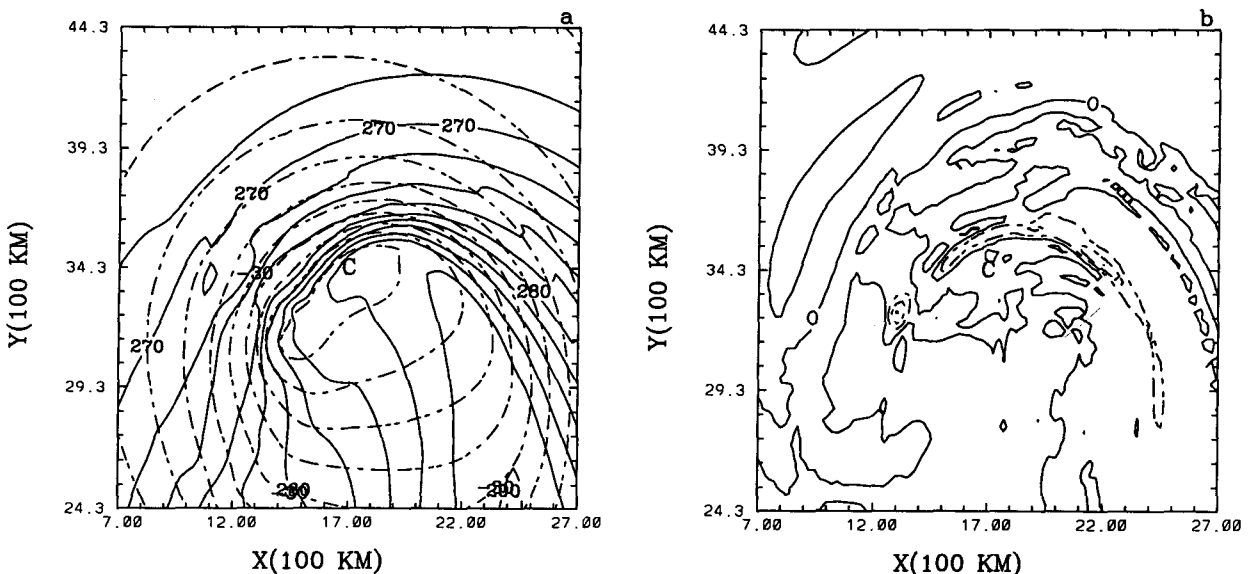


FIG. 6. Same as Fig. 5 except at 45 h. Note that the contour interval for (b) is 1.0 Pa s<sup>-1</sup>.

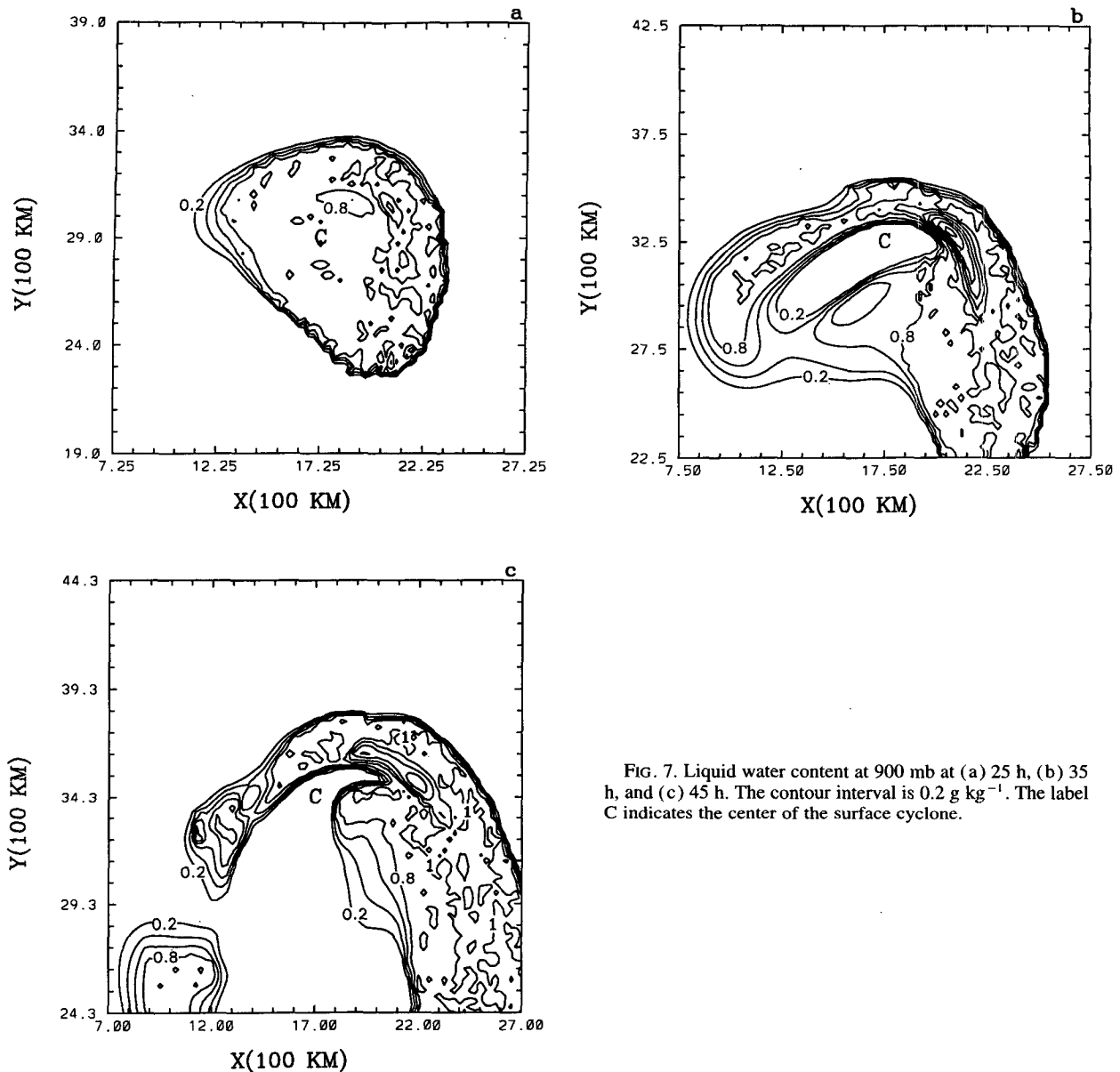


FIG. 7. Liquid water content at 900 mb at (a) 25 h, (b) 35 h, and (c) 45 h. The contour interval is  $0.2 \text{ g kg}^{-1}$ . The label C indicates the center of the surface cyclone.

the cyclone center (Fig. 8b). Slantwise convective adjustment in the warm frontal region can be noticed from the “buckling” in the angular momentum surface (Holt and Thorpe 1991; Thorpe and Clough 1991) in the warm frontal region at 600 mb. Buckling in the  $\theta_e$  surfaces is also noted, and this buckling results in upright potential instability above the region of adjustment (Bennetts and Hoskins 1979; Hedley and Yau 1991; Kuo et al. 1991a; Innocentini and Neto 1992; Persson and Warner 1993). At 45 h, the adjustment appears to be complete in the warm frontal region where the angular momentum surfaces are parallel to the  $\theta_e$  surfaces.

The occurrence of descending motion over the center of the cyclone is depicted in Fig. 9. Note that upward

motion in region of convection is flanked by unsaturated subsiding motion on either sides. The strong narrow up/downdraft couplet near  $y = 3800 \text{ km}$  and  $p = 600 \text{ mb}$  (Fig. 9b) is caused by the evaporation of cloud water in a region of compensating downward motion. This phenomenon is consistent with the results of Bennetts and Hoskins (1979), Innocentini and Neto (1992), and Persson and Warner (1993) in their numerical simulation of slantwise convection. Innocentini and Neto also noted that the evaporation of rainwater drives an unstable downdraft on the warm side and increases the convergence in the low levels.

Based on the above results, we suggest that the *descent above the slanted updraft*, augmented by evaporation of rain in the downdraft, is responsible for the

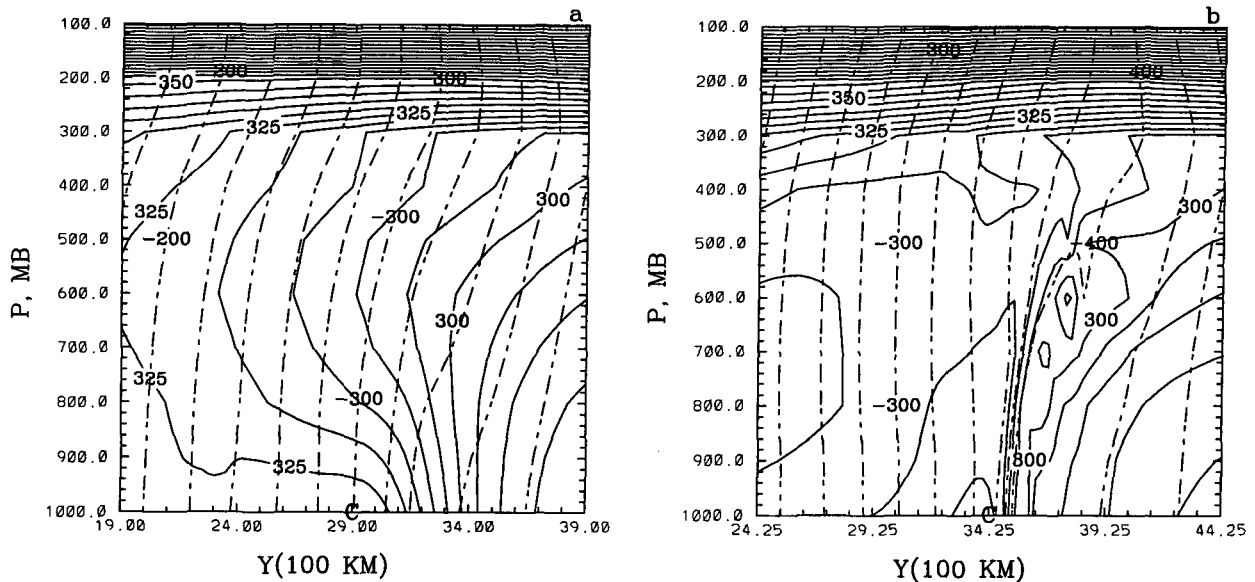


FIG. 8. Meridional cross section of angular momentum ( $m = u - fy$ ) (dashed, every  $20 \text{ m s}^{-1}$ ) and equivalent potential temperature  $\theta_e$  (solid, every  $5 \text{ K}$ ) at (a) 25 h and (b) 45 h. The section passes through the center of the cyclone denoted by the label C.

creation of *descending motion* over the cyclone center in the early stages. To test the hypothesis that the descent is convection induced, an experiment was conducted in which the latent heat due to condensation (evaporation) was not included in the temperature equation. The results indicate the absence of the depletion of liquid water around the cyclone center, which was located within a region of ascent even at 50 h. We remark that the anelastic modeling of explosive cyclogenesis by Hedley and Yau (1991) also shows that the low-level air to the west of the cyclone center first descends slightly before being carried upward in the warm frontal zone. Downward motion of about  $0.5 \text{ m s}^{-1}$  was diagnosed on the warm side of the westward extension of the bent-back warm front in the seclusion phase of the ERICA IOP4 storm (Neiman and Shapiro 1993a,b).

To examine the stability properties of the bent-back warm front, east–west oriented vertical cross sections passing through the cyclone center at 45 h are shown in Fig. 10. The fields plotted include angular momentum  $m = v + fx$ , equivalent potential temperature  $\theta_e$ , potential temperature  $\theta$ , and vertical velocity  $\omega$ . Note that the atmosphere has developed neutrality to slantwise convection to the west of the cyclone center in the bent-back warm frontal region (Fig. 10a). The buckling in the angular momentum surfaces at 700 mb along the bent-back warm front indicates slantwise convective overturning. To the east of the cyclone center, the atmosphere is potentially unstable to vertical convection and slantwise neutrality is again present in the warm frontal zone. The mesoscale nature of the upward and downward motions due to the slantwise convection

in the frontal regions (Fig. 10b) is consistent with the results reported in Hedley and Yau (1991) and BY94.

#### b. PV diagnostics

To quantify the contribution to cyclogenesis by surface thermal advection, latent heat release from vertical/slantwise convection, and vorticity advection due to the upper-level wave, we invert the potential vorticity (PV) anomaly arising from each of these physical processes.

For a fully baroclinic, compressible fluid, the EPV is given by

$$q = -g(f\mathbf{k} + \nabla \times \mathbf{V}) \cdot \nabla \theta. \quad (12)$$

Ertel PV is a conserved quantity following the motion in an inviscid flow in three dimensions (Rossby 1940; Ertel 1942). If the flow is quasigeostrophic,  $q$  becomes the quasigeostrophic pseudopotential vorticity (PPV) of Charney and Stern (1962). Then the right-hand side of (12) is linear in the streamfunction  $\psi$ , which can be solved through an inversion of PPV. Furthermore, any atmospheric state can be decomposed into the sum of a mean variable and a set of individual anomalies. For the mean PPV and for each of its anomalies, (12) can be inverted given the quasigeostrophic balance constraint between wind and mass to yield the associated circulation (Hoskins et al. 1985). By further invoking the superposition principle, the total circulation can be obtained by adding the individual circulations associated with each anomaly in  $q$ . An analogy can be drawn from electromagnetic theory where given a specific charge distribution, one can solve for the potential in-

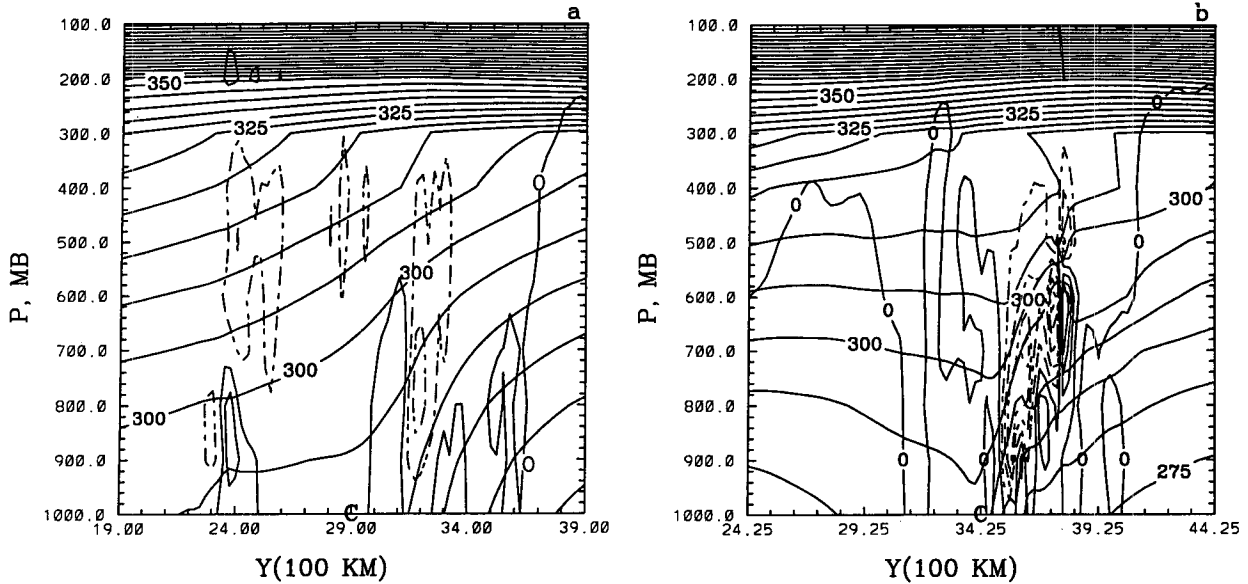


FIG. 9. Same as Fig. 8 but for potential temperature (solid, every 5 K) and vertical velocity at every  $0.5 \text{ Pa s}^{-1}$  at (a) 25 h and (b) 45 h.

side the domain of interest as a boundary value problem. The linear relation in electrostatics allows the superposition of potentials due to each individual charge at any point.

If the quasigeostrophic assumption is not made, the right of (12) is no longer linear in  $\psi$  and the nonlinearities preclude an exact invertibility statement of EPV. However, DE91 and Davis (1992a) developed an inversion procedure based on the relative smallness

of the irrotational part of the horizontal wind. Their method is adopted in our analysis and we present a summary of the method and the solution techniques in the appendix.

*c. Results from PV diagnostics*

To delineate clearly the effect of convection on explosive cyclogenesis, we will compare the results of the

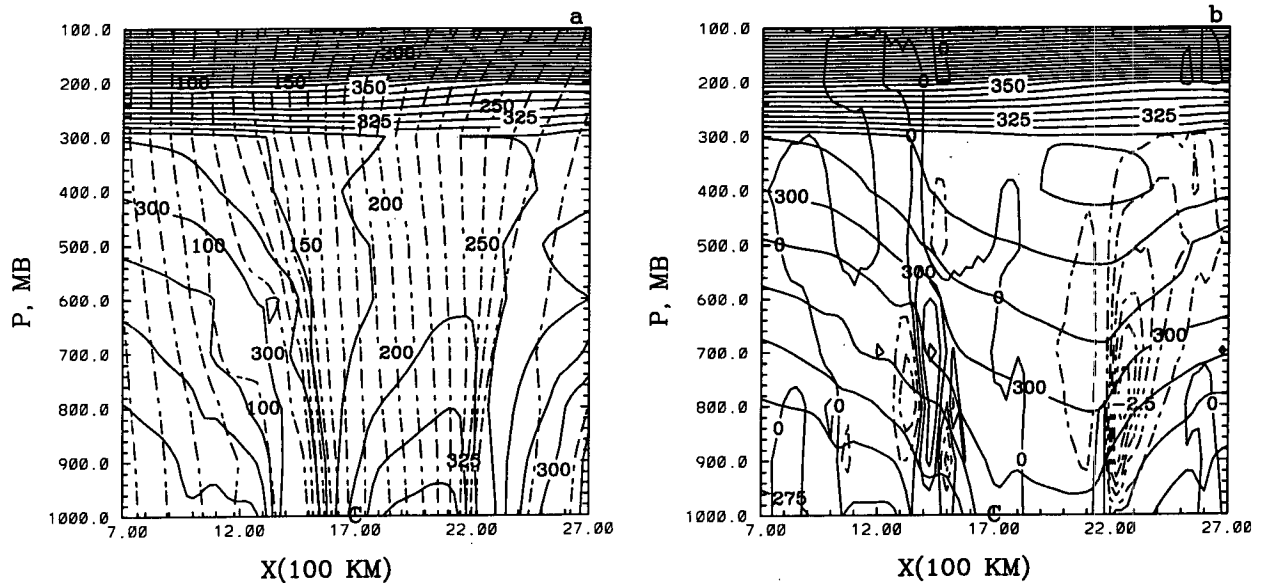


FIG. 10. Zonal cross sections at 45 h of (a) angular momentum ( $m = v + fy$ ) (dashed, every  $10 \text{ m s}^{-1}$ ) and equivalent potential temperature  $\theta_e$  (solid, every 5 K), and (b) potential temperature (solid, every 5 K) and vertical velocity (every  $0.5 \text{ Pa s}^{-1}$ ). The section passes through the center of the cyclone denoted by the label C.

inversion of EPV anomalies for the moist and dry cyclones. The mean flow is chosen to be given by the basic state with a zonal jet and a geostrophically balanced mass field. Figure 11a depicts the computed mean EPV. Small values less than 1 PVU are noted in the troposphere, but the stratosphere is evidently a reservoir of the high EPV. The mean geopotential and the mean streamfunction needed for the FL method are obtained from the inversion of the mean EPV given the potential temperature at 1000 mb (Fig. 11b) and at 100 mb.

Since the moist cyclone reaches its mature stage at 45 h, it is appropriate to invert the PV anomalies at this time. The anomalies are obtained by subtracting the mean values from the total values (refer to the appendix for details). No flux boundary conditions are applied at the north–south walls for the inversion process. Following DE91, three anomalies are considered: 1) the 1000-mb  $\theta$  anomaly ( $\theta_B$ ), which if positive is equivalent to a positive EPV anomaly with an associated cyclonic vorticity (Hoskins et al. 1985); 2) low-level perturbation potential vorticity (LPV), which comprises the anomalies at the grid points between 900 and 600 mb; and 3) the upper-level perturbation potential vorticity (UPV), which consists of the anomalies at the grid points from 500 to 200 mb. For convenience, we include in the flow associated with the UPV the circulation given by the 100-mb  $\theta$  anomaly.

The physical mechanism responsible for the  $\theta_B$  anomaly is warm and cold advection in the lower atmosphere during the development of the baroclinic wave. Diabatic processes like surface heat flux can also contribute to  $\theta_B$ . However, their contribution appears small as sensitivity experiments with and without sur-

face heat fluxes in a dry cyclone indicate similar results in agreement with earlier findings of Reed et al. (1992).

In dry cyclogenesis the only physical mechanism that creates LPV is the advection of mean tropospheric PV if a gradient exists. On the contrary, in a moist cyclone condensation in a region of cyclonic vorticity creates positive (negative) PV below (above) the level of maximum vertical velocity (Reed et al. 1992).

Normally, high values of PV are found in the upper-level troughs. In vertical cross sections, the troughs appear as depressions in the tropopause and hence possess PV values typical of the stratosphere. The physical mechanism for the interaction of UPV with the low-level system is vorticity advection.

Figures 12 and 13 display the surface  $\theta$  anomaly and EPV anomalies at the 800-mb and 300-mb levels for the dry and moist cyclones, respectively, at 45 h. The 1000-mb potential temperature anomaly over the cyclone center,  $\theta_B$ , is weaker in the moist case (Figs. 12a and 13a) and, as will be demonstrated later, is related to the convection-induced cold advection in the bent-back warm frontal region. The 800-mb EPV anomaly is negative in the warm frontal zone (Fig. 12b) for the dry cyclone but is strongly positive in the region of the warm front and the bent-back warm front in the moist run (Fig. 13b). This positive anomaly originates from latent heat release as a result of vertical/slantwise convection.

At 300 mb, a positive–negative EPV anomaly couplet, associated with the trough–ridge pattern, is present in both cases (Figs. 12c and 13c). The ridge in the moist case possesses a much stronger negative EPV anomaly in comparison to the dry cyclone. This result

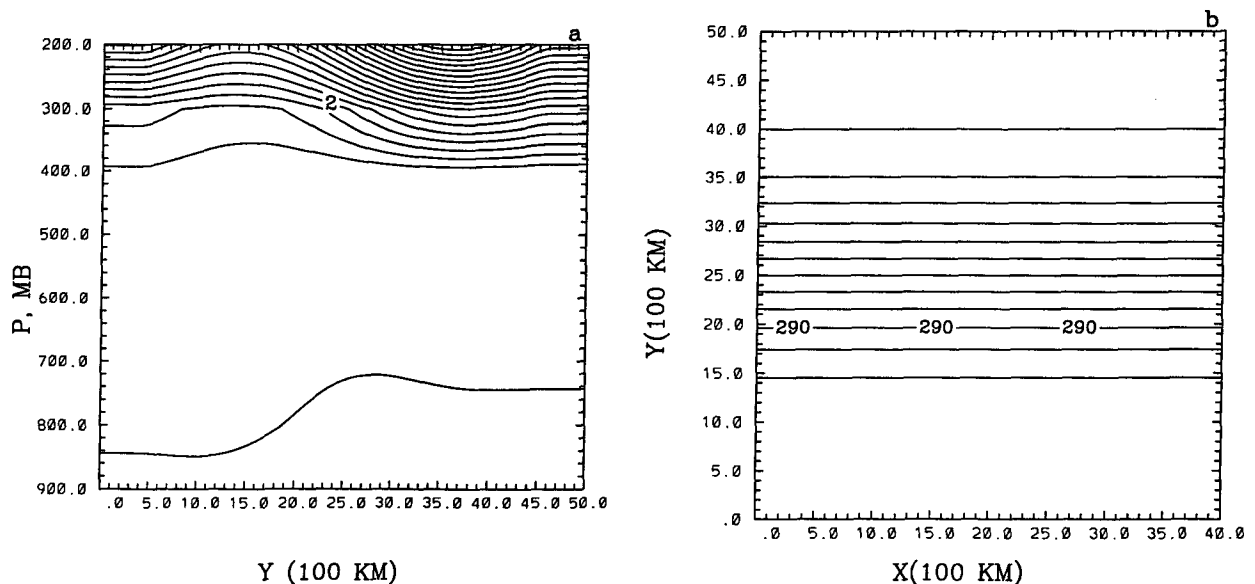


FIG. 11. (a) The basic-state potential vorticity every 0.5 PVU, and (b) the mean surface (1000 mb)  $\theta$  every 2 K.

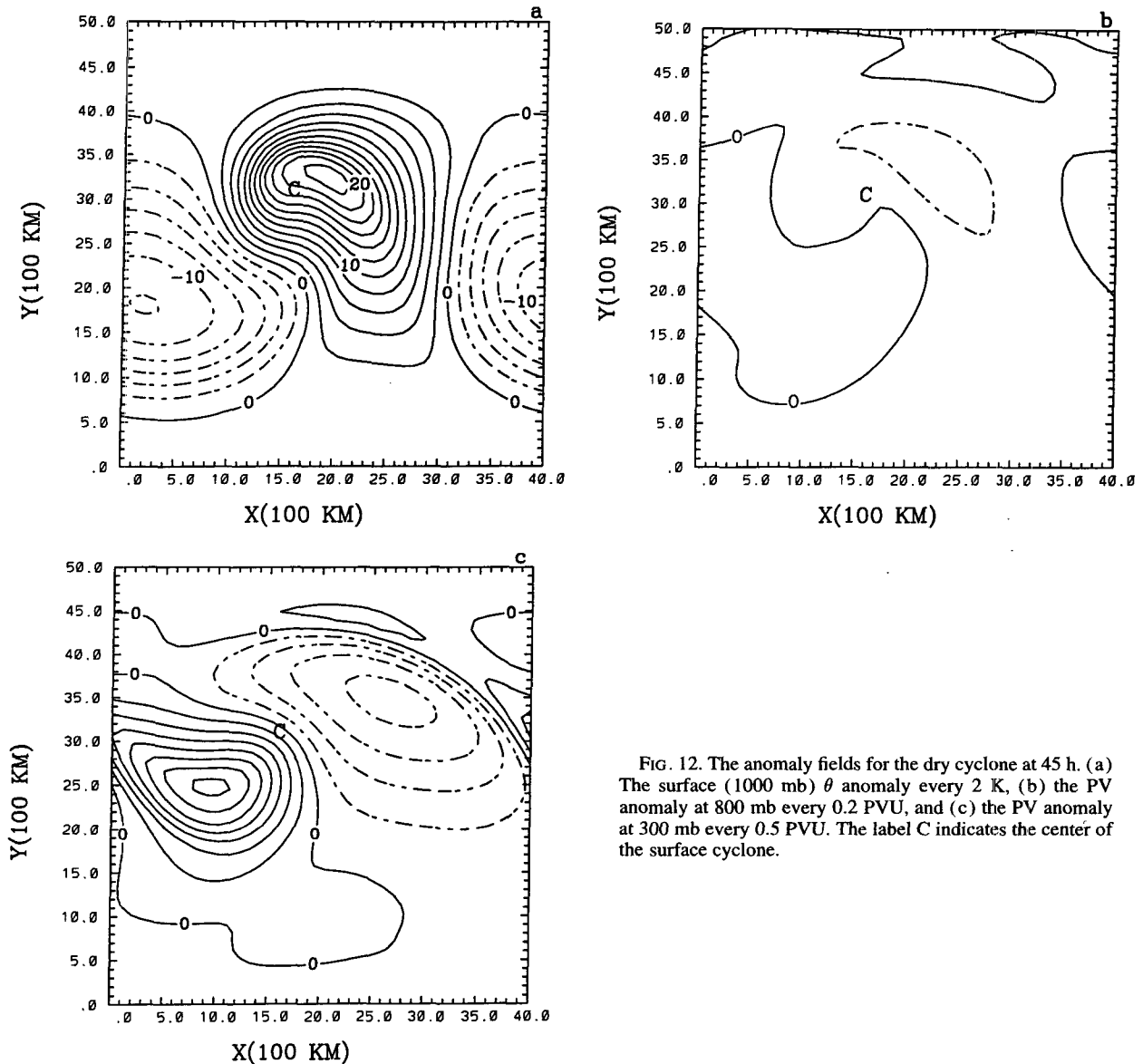


FIG. 12. The anomaly fields for the dry cyclone at 45 h. (a) The surface (1000 mb)  $\theta$  anomaly every 2 K, (b) the PV anomaly at 800 mb every 0.2 PVU, and (c) the PV anomaly at 300 mb every 0.5 PVU. The label C indicates the center of the surface cyclone.

is consistent with the view presented in Eliassen and Kleinschmidt (1957), who showed that the strong vertical motion associated with latent heat release produces negative EPV above the updraft maxima and positive EPV below. The negative EPV is then transported upward by the "warm conveyor belt" into the ridge region at the upper levels, while the positive EPV is transported to the west of the cyclone center by the "cold conveyor belt." Note also that in the moist case, the maximum positive anomaly in the region of the trough exceeds the dry cyclone by 0.265 PVU, suggesting a stronger wave development at the upper levels.

To quantify the effects of various physical processes to cyclogenesis, we computed the geopotential pertur-

bations at 900 mb associated with the EPV anomalies at different levels. Figures 14 and 15 depict the results at 45 h for the dry case and moist case, respectively. The inversion is quite accurate as the difference between the total 900-mb geopotential perturbation obtained from the numerical model and from the inversion method is only about 1 dm (not shown).

A notable feature in the inverted geopotential field associated with  $\theta_B$  is the crowding of contours (Fig. 15a) to the north of the moist cyclone. This crowding is associated with the strong thermal gradient in that region (Fig. 13a). In the dry run (Fig. 14a), the cyclone center is almost collocated with the minimum in the geopotential perturbation. The amplitude of the inverted field is also stronger, and we will later show that

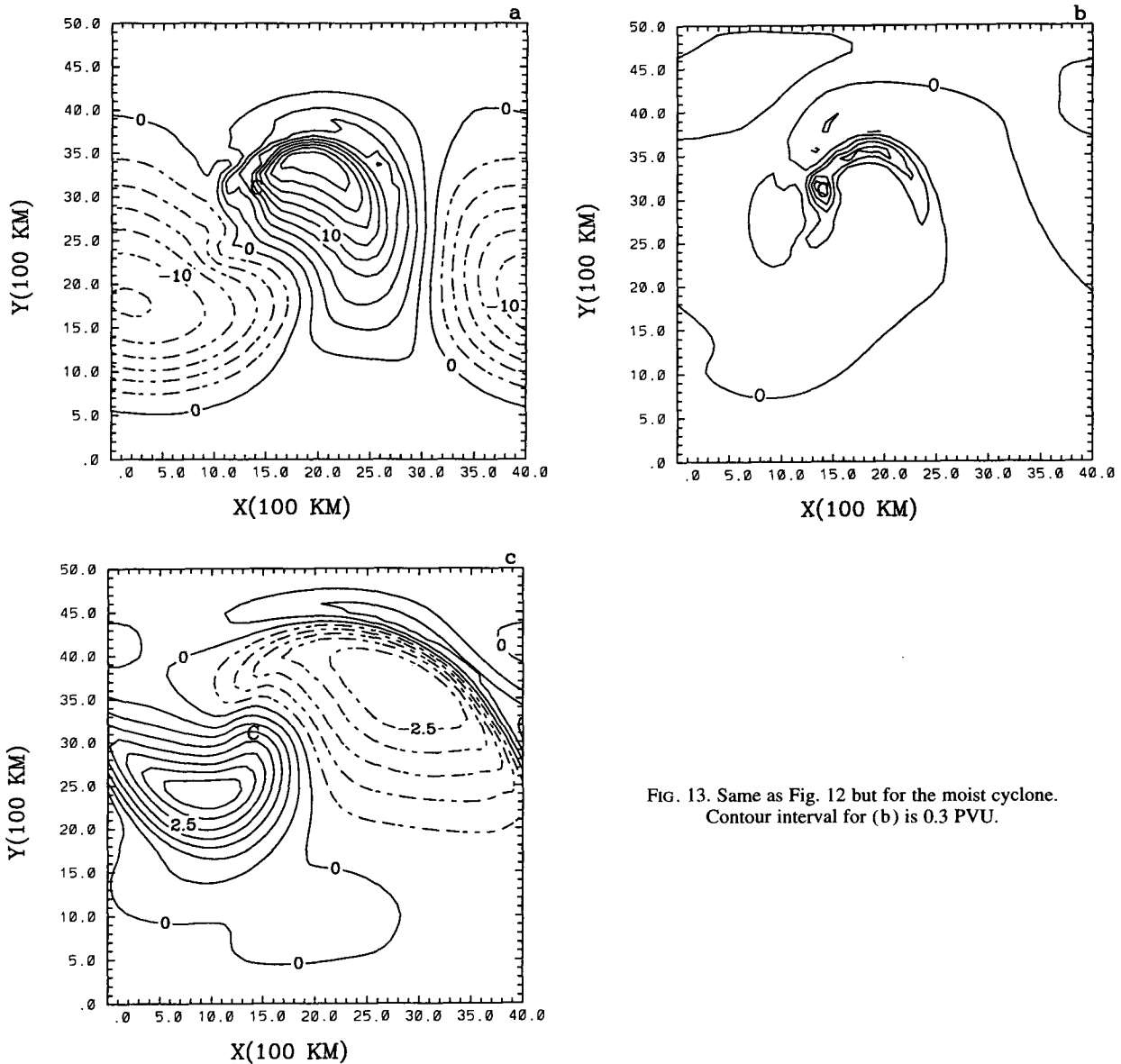


FIG. 13. Same as Fig. 12 but for the moist cyclone. Contour interval for (b) is 0.3 PVU.

this arises from the absence of cold advection associated with the LPV in the region of the bent-back warm front.

The inverted geopotential perturbation due to LPV (Fig. 14b) is quite weak in the dry model. However, in the moist model (Fig. 15b), its magnitude is comparable to the perturbation associated with  $\theta_B$  and the center of the cyclone is located directly over the center of the perturbation. The effect of convection in the region of the warm front and bent-back warm front is also evident from the strong gradients. The perturbation due to UPV indicates larger values in the moist cyclone whose center is also closer to the center of the perturbation (Figs. 14c and 15c).

The characteristics of the forcing and the geopotential perturbation at 900 mb can be interpreted in terms of the 900-mb nondivergent wind retrieved from the inversion process and the potential temperature at the same level. In both the dry (Fig. 16a) and moist (Fig. 17a) cyclones, the wind field due to  $\theta_B$  displays the classic pattern of warm advection to the northeast and cold advection to the southwest of the cyclone center. The magnitude of the wind is somewhat larger in the dry case. The wind field associated with the LPV (Fig. 16b) for the dry cyclone shows an anticyclonic circulation in the warm frontal region and an overall pattern of warm advection. In contrast, the warm advection in the moist cyclone (Fig. 17b) is accompanied by an

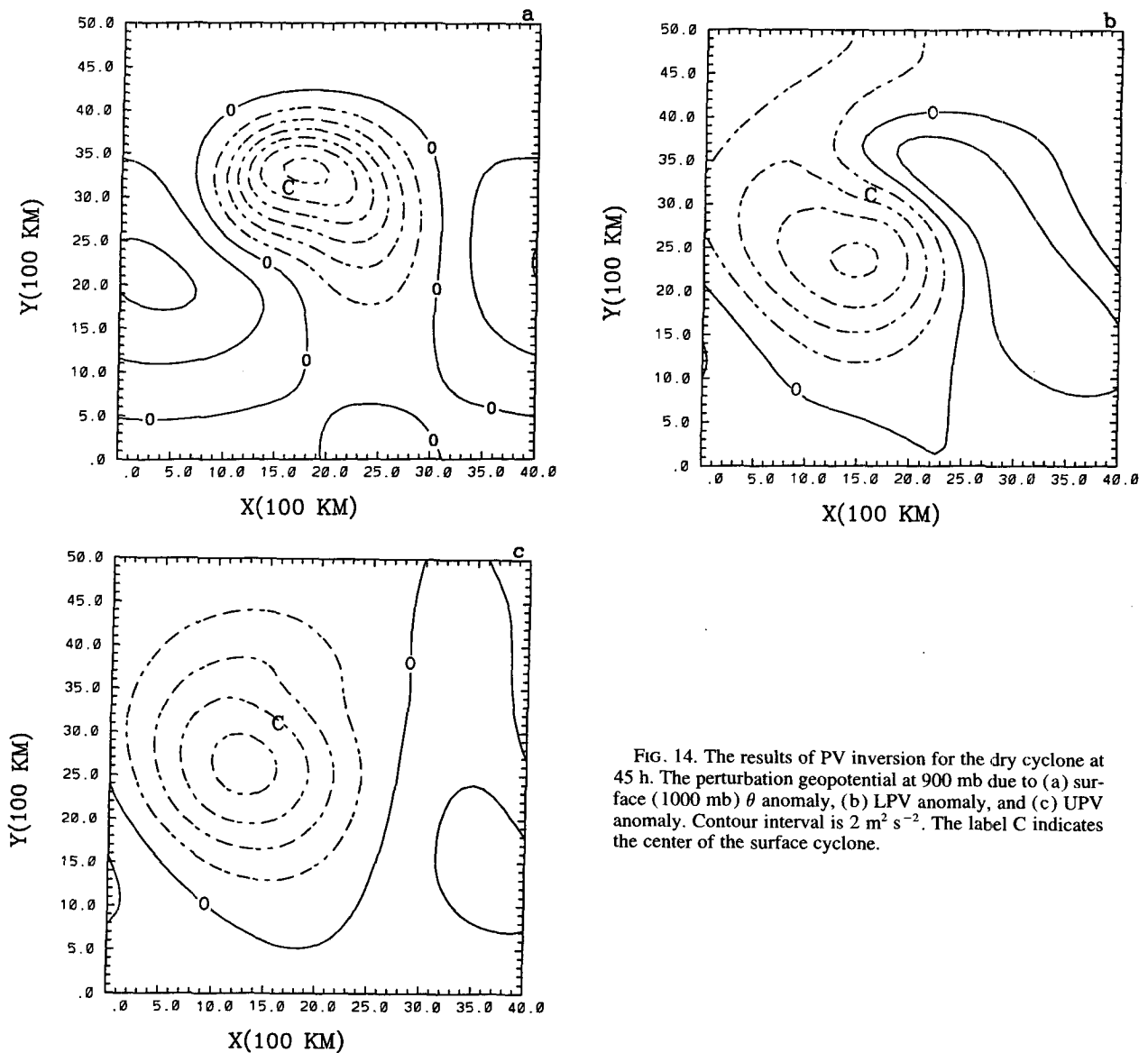


FIG. 14. The results of PV inversion for the dry cyclone at 45 h. The perturbation geopotential at 900 mb due to (a) surface (1000 mb)  $\theta$  anomaly, (b) LPV anomaly, and (c) UPV anomaly. Contour interval is  $2 \text{ m}^2 \text{ s}^{-2}$ . The label C indicates the center of the surface cyclone.

overall cyclonic circulation around the cyclone center. A distinct small-scale cyclonic circulation associated with a positive EPV anomaly (Fig. 13b) appears in the region of the bent-back warm front, resulting in cold temperature advection to the southwest of the cyclone center. The cold advection associated with the LPV reduces the strength of the  $\theta_B$  anomaly in the moist cyclone. The circulations associated with the UPV anomaly (Fig. 16c and 17c) exhibit similar characteristics for the two cases.

The contributions of  $\theta_B$ , LPV, and UPV to the geopotential perturbations at 900 mb, 500 mb, and 300 mb over the cyclone center are summarized in Table 3. At 900 mb, the  $\theta_B$  forcing accounts for 74.2% of the height fall in the dry cyclone. In contrast, height fall associated

with the LPV is most important in the moist case. The UPV contribution is 4.3 dam higher in the moist cyclone, and it suggests an enhanced influence of the upper-level wave in moist cyclogenesis.

At 500 mb, both the LPV and UPV contributions in the moist run exceed the dry run by at least a factor of 2. At 300 mb, the contribution of surface  $\theta$  anomaly is insignificant in both cases. Again the contributions from LPV and UPV are at least doubled in the moist cyclone.

Our results from the EPV inversion are in agreement with the scenario for the enhanced deepening of some oceanic cyclones proposed by BY94. We showed therein that the release of potential instability by convection and nonlinear advection results

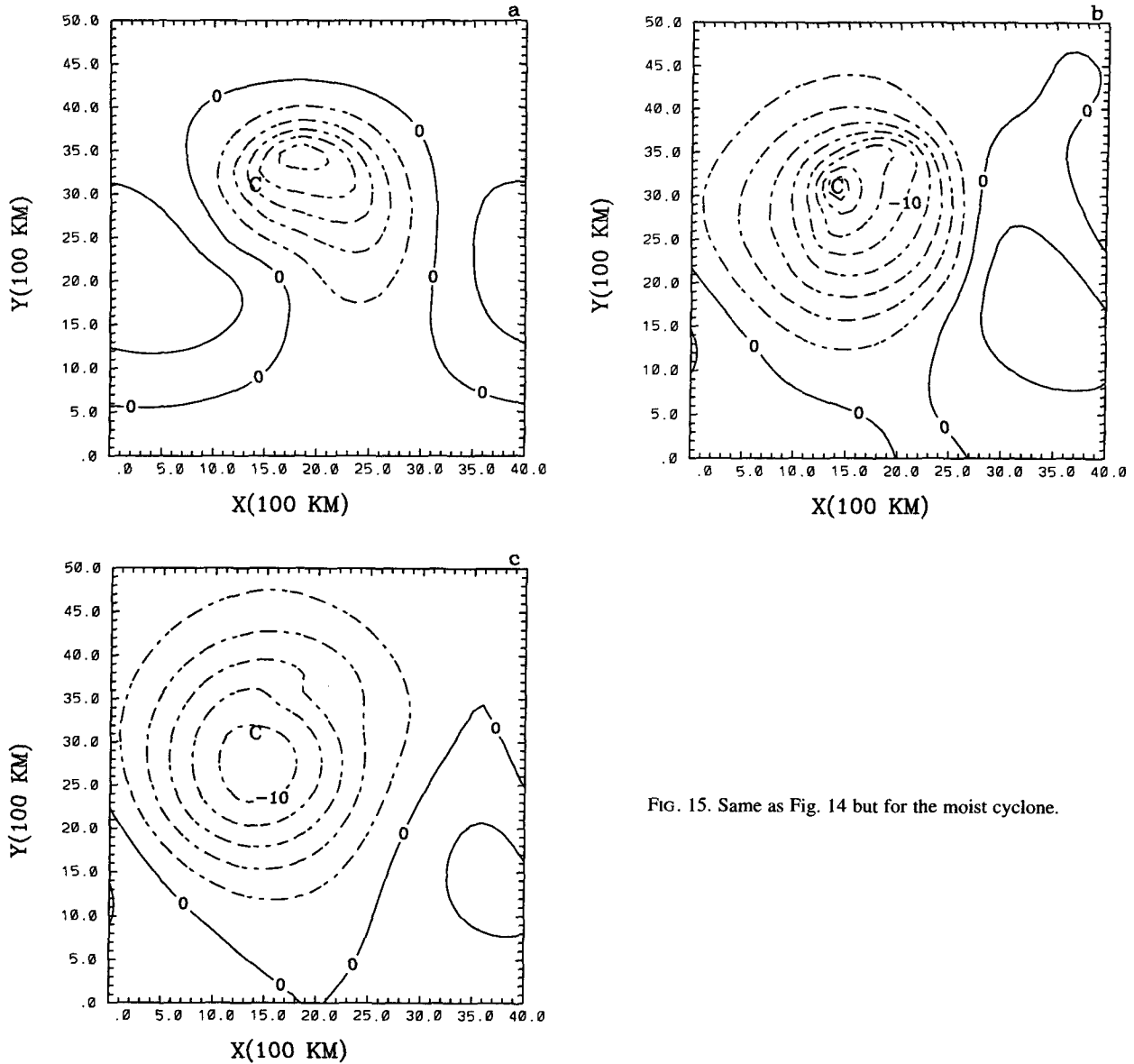


FIG. 15. Same as Fig. 14 but for the moist cyclone.

in rapid warm frontogenesis and the formation of the bent-back warm front. A sudden intense cold advection breaks out to the west and southwest of the cyclone center and the upper-level trough intensifies dramatically. Strong upper-level vorticity advection ensues and the surface system deepens explosively.

A similar picture is indicated in Fig. 18, where we plotted the averaged thermal advection over a 525 km × 525 km area located to the southwest of the cyclone with the storm center at the top right corner. The advection is calculated in a frame moving with the cyclone. Warm advection is indicated in the dry case over the entire period of the simulation (Fig. 18a). In the moist run (Fig. 18b), however, warm advection starts

to decrease at 25 h and cold advection dominates below 300 mb after 30 h. This cold advection decreases the  $\theta_B$  anomaly and the height fall at 900 mb associated with  $\theta_B$  relative to the case of the dry cyclone.

Figure 19 shows the averaged vorticity advection at 500 mb and 300 mb over an area of dimensions 525 km × 525 km located immediately to the northeast of the cyclone with the storm center in its lower left corner. The calculation is again in a frame moving with the center of the cyclone. A sharp rise in vorticity advection at 25 h can be noted in the moist case, reaching a value as high as  $4.3 f \text{ day}^{-1}$  at 500 mb. On the contrary, vorticity advection shows a gentle rise at both 500 mb and 300 mb in the dry case. This is consistent with the enhanced effect of

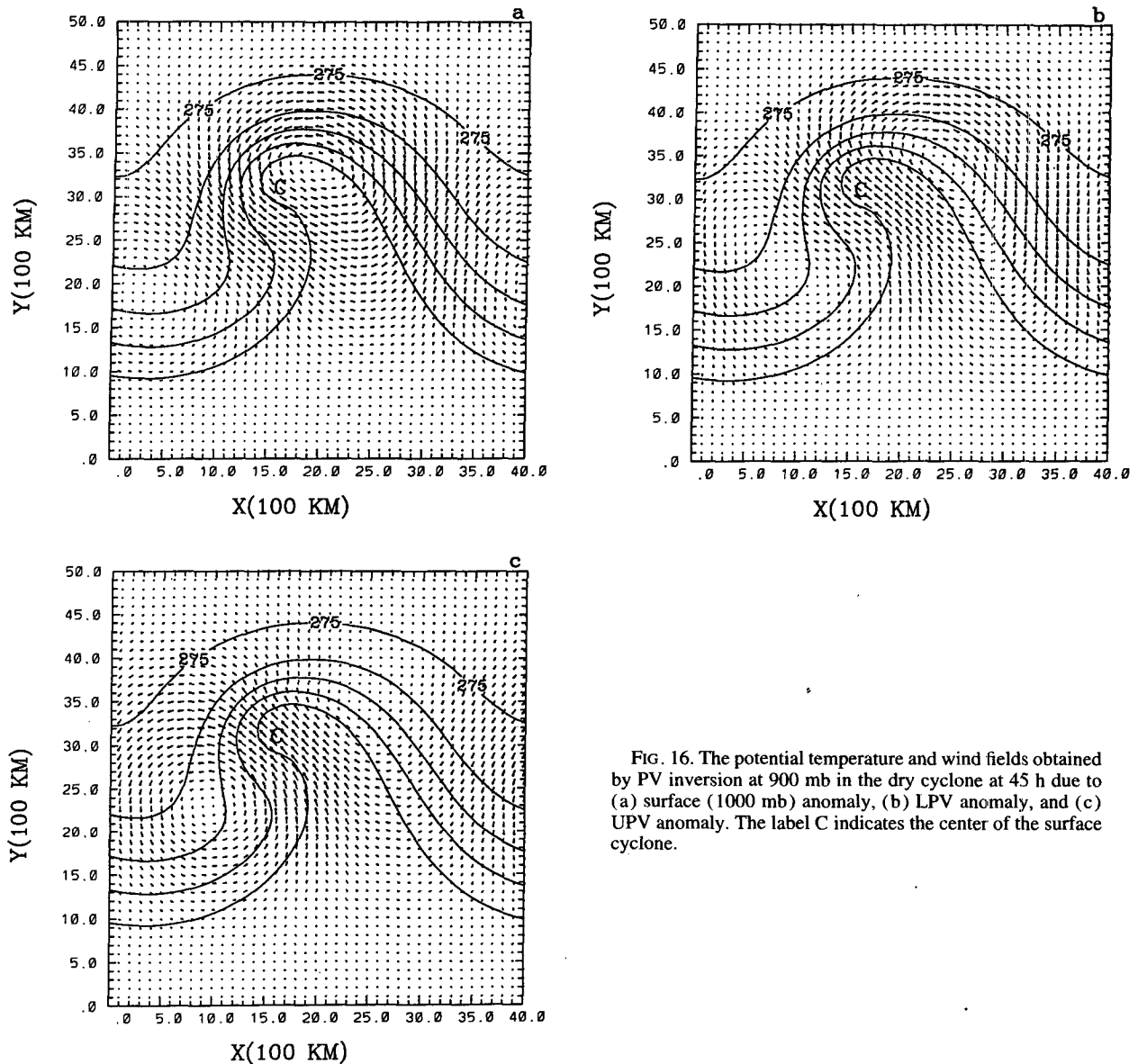


FIG. 16. The potential temperature and wind fields obtained by PV inversion at 900 mb in the dry cyclone at 45 h due to (a) surface (1000 mb) anomaly, (b) LPV anomaly, and (c) UPV anomaly. The label C indicates the center of the surface cyclone.

the circulations associated with the LPV and the UPV in the EPV analysis.

In passing, we remark that our results bear similarities to and differences from those obtained by Davis. DE91 and Davis (1992b) analyzed two continental cyclones on 5 February 1988 and 15 December 1987 and found that LPV accounts for 40% and 20% of the contribution to cyclogenesis in the two storms, respectively. Davis et al. (1993) presented the difference fields between a moist run and a dry run. The cyclonic circulation and the cold advection in the bent-back warm frontal region can also be noted. However, their results did not reveal the mesoscale structures due to convection. Furthermore, Davis (1992b) suggested condensation can have a cyclolytic effect by inducing

a circulation that hastens the propagation of the thermal wave at lower levels to the northeast, thereby separating the tropopause and surface PV anomalies leading to a decay of the disturbance. In our work, we view the cyclolytic effect as a result of the encroachment of cold advection into the storm center resulting in a reduction of the warm anomaly at the center of the cyclone.

#### 4. Conclusions

The primary motivation of this paper has been to extend the previous results of BY94 to a multilevel model with explicit condensation and to quantify the contribution of convection, both slantwise and vertical, to marine cyclogenesis. To this end, we simulated an

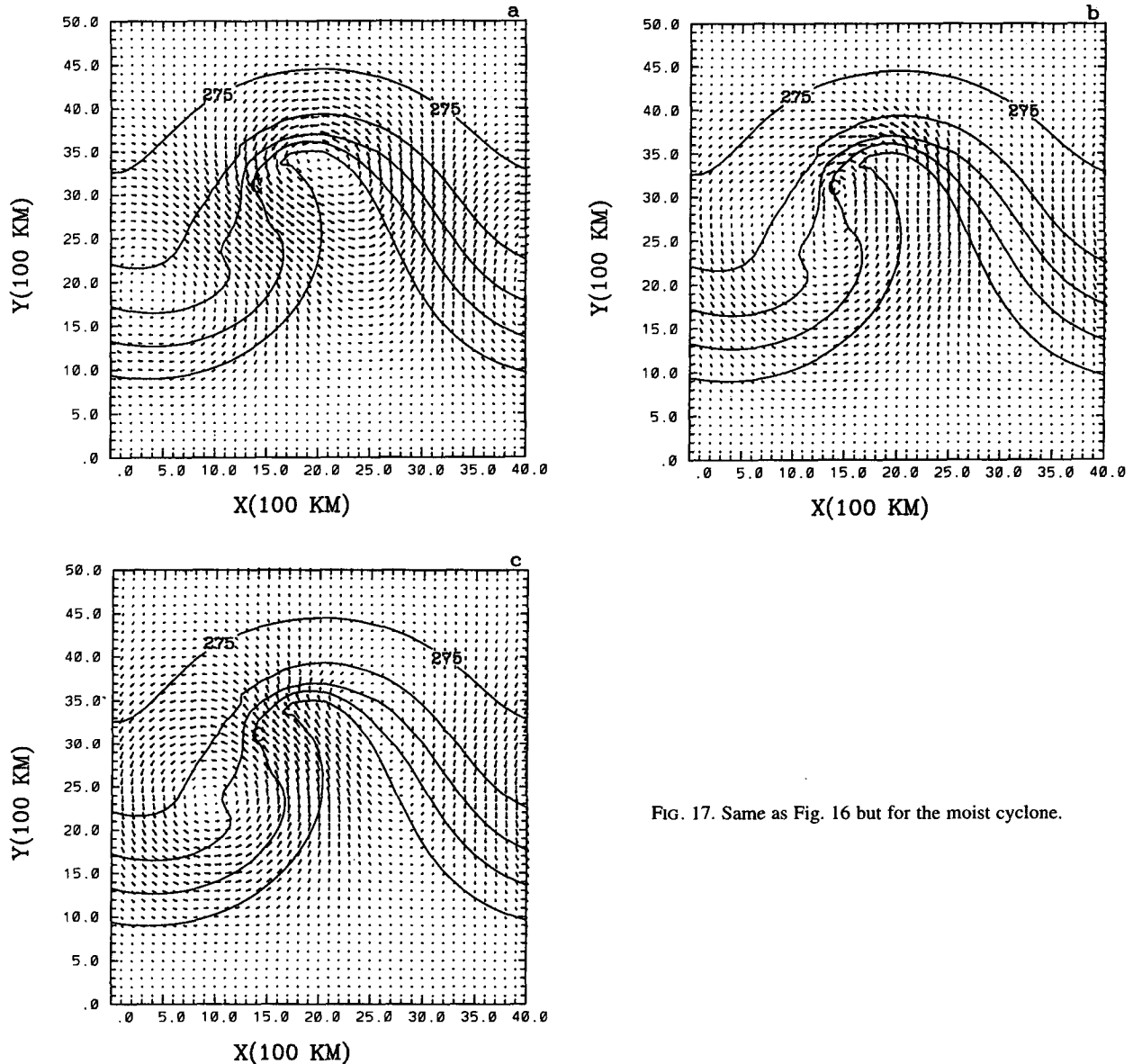


FIG. 17. Same as Fig. 16 but for the moist cyclone.

explosive cyclone with idealized initial conditions. The moist cyclone differed significantly from the dry cyclone with the formation of an intense warm front to the north of the cyclone center. The warm front adjusted to slantwise neutrality during the explosive deepening period and wrapped around the cyclone center to form the bent-back warm front. Cross-section analysis indicates slantwise neutrality in both the warm front and the bent-back warm front.

Beginning from the early stages of cyclogenesis, the horizontal liquid water field shows the development of a dry slot over the cyclone center. The vertical velocity field also shows descent over the center of the cyclone to the south of the intense warm front where vigorous uplifting occurred. Based on previous modeling studies

on slantwise convection and explosive cyclogenesis and recent observational findings, we suggest that the dry slot is created by the descending branch of slantwise convection on the warm side of the warm front. The descent is augmented by the evaporation of liquid water as in an experiment in which the heat due to condensation (evaporation) was not added (subtracted) to (from) the thermodynamic equation, the cyclone center was in a region of ascent even at the mature stage.

The piecewise inversion technique from DE91 is used to invert the EPV anomalies in the mature stage of the moist and dry cyclones. We calculate specifically the perturbation geopotential at 900, 500, and 300 mb over the cyclone center due to EPV anomalies at dif-

TABLE 3. Contribution of  $\theta_B$ , LPV, and UPV to the 900-mb, 500-mb, and 300-mb perturbation geopotential fields over the cyclone center at 45 h for the dry and moist cyclones.

Level (mb)	Perturbation $\phi$ (dam)	Contributions from		
		$\theta_B$ (dam) (%)	LPV (dam) (%)	UPV (dam) (%)
Dry				
900	-31.8	-23.6 (74.2)	-2.5 (7.9)	-5.7 (17.9)
500	-12.5	-4.3 (34.4)	-3.7 (29.6)	-4.5 (36)
300	-5.0	-0.6 (12)	-2.1 (42)	-2.3 (46)
Moist				
900	-41.8	-14.9 (35.6)	-16.9 (40.4)	-10.0 (24)
500	-21.4	-3.7 (17.3)	-8.7 (40.7)	-9.0 (42)
300	-12.2	-1.0 (8.2)	-4.0 (32.8)	-7.2 (59)

ferent levels. The warm and bent-back warm frontal regions in the moist cyclone exhibit a thin band of positive EPV anomaly while the dry cyclone shows negative values in the same region. The LPV, which includes the anomalies between 900 and 600 mb, contributes 40% to the total geopotential perturbation at the moist cyclone center. Its contribution to perturbation geopotential at 500 mb over the moist cyclone center is twice that in the dry case. The circulation of the inverted nondivergent wind fields in the moist cyclone shows a small-scale cyclonic vortex and the presence of cold advection in the bent-back warm frontal region.

The UPV, which includes the anomalies between 500 and 100 mb, also makes enhanced contribution to the 900-mb perturbation geopotential over the moist center of the moist cyclone. The enhanced contribution is traced to an increase in the vorticity advection in the midtroposphere in association with cold advection in the bent-back warm front. The contribution of 1000-mb  $\theta$  anomaly to the mature moist cyclone, in comparison to the dry one, is reduced due to the negative impact of the cold advection associated with the LPV in the bent-back warm frontal region.

The role of convection in the conceptual picture suggested by BY94 is in agreement with the PV inversion results. The bent-back warm front in the moist cyclone is a region of cold advection in BY94. The inversion of LPV indicates that the individual circulation due to condensation is producing cold advection in the moist cyclone while the dry cyclone shows a broad warm advection in the same region. Vorticity advection aloft increases in association with cold advection in BY94 and in the present model. In addition to this positive

impact on cyclogenesis, the present work shows that convection has the negative effect of decreasing the magnitude of the surface  $\theta$  anomaly near the cyclone center.

In closing, we remark that there are a number of limitations in the model that need to be improved. Principal among these are the coarse-grid resolution and the treatment of the planetary boundary layer. A 25-km horizontal grid spacing can resolve some form of slantwise convection (Persson and Warner 1993) but may be inadequate in resolving the most unstable mode. Similarly, the effects of upright convection and evaporation-induced downdrafts on the storm might not be

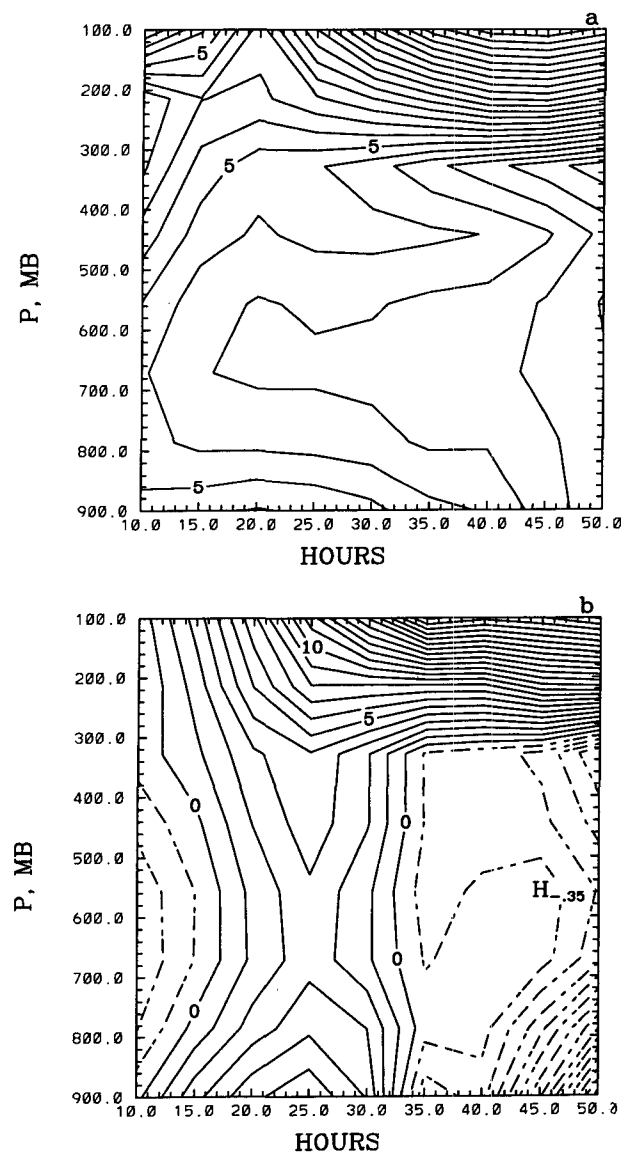


FIG. 18. The quasi-Lagrangian thermal advection averaged over a 525 km  $\times$  525 km area southwest of the cyclone center for (a) the dry cyclone and (b) the moist cyclone. Contour interval is 1 K day $^{-1}$ .

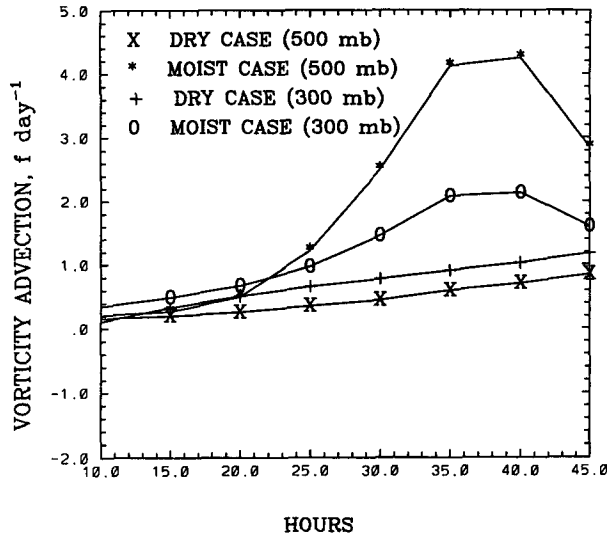


FIG. 19. The quasi-Lagrangian relative vorticity advection at 500 mb and 300 mb averaged over a 525 km  $\times$  525 km area northeast of the cyclone center.

represented *accurately*. In addition, the use of the bulk aerodynamic formulation for boundary-layer heat and moisture transports yields only a first-order effect. Despite these shortcomings, it was gratifying to find that the model simulated some realistic features of explosive cyclones and the results are consistent with those obtained in an anelastic model using a 10-km horizontal grid spacing (Hedley and Yau 1991). Further experiments using a fully compressible model with high spatial resolutions and detailed planetary boundary-layer physics will be carried out in the near future.

**Acknowledgments.** This research was supported by the U.S. Office of Naval Research Grant N00014-87-G-0171, the Atmospheric Environment Service, and the National Science and Engineering Research Council of Canada. G. Balasubramanian is also supported by a McGill/CIDA fellowship. The authors thank Dr. Dan Keyser for interesting discussions.

#### APPENDIX

##### Inversion of PV

Following Davis and Emanuel (1991), we outline briefly the fully linear (FL) method of inverting EPV. The basic assumption is that the irrotational component of the wind is very small relative to the nondivergent wind. A streamfunction  $\psi$  can then be defined and (12) can be approximated as

$$q = \frac{g\kappa\pi}{p} \left[ (f + \nabla^2\psi) \frac{\partial^2\phi}{\partial\pi^2} - \frac{\partial^2\psi}{\partial\pi\partial x} \frac{\partial^2\phi}{\partial\pi\partial x} - \frac{\partial^2\psi}{\partial\pi\partial y} \frac{\partial^2\phi}{\partial\pi\partial y} \right], \quad (\text{A1})$$

where  $\kappa = R/C_p$  and  $\pi = C_p(p/p_0)^\kappa$ . By adopting the balance equation of Charney (1955),

$$\nabla^2\phi = \nabla \cdot f \nabla \psi + 2 \left[ \frac{\partial^2\psi}{\partial x^2} \frac{\partial^2\psi}{\partial y^2} - \left( \frac{\partial^2\psi}{\partial x\partial y} \right)^2 \right], \quad (\text{A2})$$

$\psi$  can be solved from (A1) and (A2) for a given distribution of  $q$  with appropriate boundary conditions. McWilliams (1985) has shown that the balance equation is quite accurate as long as the Froude number is small, even when the Rossby number is  $\gg 1$ .

For the boundary conditions, we assume periodicity in the east–west direction and the following Neumann conditions at the north–south and top and bottom boundaries:

$$\begin{aligned} \frac{\partial\phi}{\partial\pi} = f \frac{\partial\psi}{\partial\pi} = -\theta, \quad \pi = \pi_0; \quad \pi = \pi_T \\ \frac{\partial\phi}{\partial y} = \frac{\partial\psi}{\partial y} = 0, \quad y = 0; \quad y = L_y, \end{aligned} \quad (\text{A3})$$

where  $\pi_T$  is the dimensionless pressure corresponding to 100 mb and  $L_y$  is the north–south domain length.

The method begins by first decomposing the total fields of EPV ( $q$ ), geopotential ( $\phi$ ), and streamfunction ( $\psi$ ) into the sum of a mean ( $q_0$ ,  $\phi_0$ , and  $\psi_0$ ) quantity and a total perturbation ( $q'$ ,  $\phi'$ , and  $\psi'$ ) quantity. The perturbation  $q'$  is made up of individual EPV anomalies  $q_n$ , and similarly other total perturbations are sums of individual perturbations associated with the  $q_n$ 's:

$$q' = \sum_1^N q_n; \quad \phi' = \sum_1^N \phi_n; \quad \psi' = \sum_1^N \psi_n. \quad (\text{A4})$$

Because  $q$  involves nonlinear products of  $\psi$  and  $\phi$ , there is no unique way to relate the anomalies  $q_n$ ,  $\psi_n$ , and  $\phi_n$ . However, DE91 proposed that if a function  $C$  is a nonlinear product of functions  $A$  and  $B$ , that is,  $C = AB$ , then a presumably least arbitrary approach is to write

$$C_n = \left( A_0 + \frac{1}{2} \sum_1^N A_n \right) B_n + \left( B_0 + \frac{1}{2} \sum_1^N B_n \right) A_n, \quad (\text{A5})$$

where  $A_0$  and  $B_0$  represent the mean values for  $A$  and  $B$ . Note the symmetry of invariance under an exchange of  $A$  and  $B$  in (A5).

By using (A5), (A1) and (A2) can be reduced to the following set of equations,

$$\begin{aligned} \nabla^2\phi_n = \nabla \cdot f \nabla \psi_n + 2 \left[ \frac{\partial^2\bar{\psi}}{\partial x^2} \frac{\partial^2\psi_n}{\partial y^2} \right. \\ \left. + \frac{\partial^2\bar{\psi}}{\partial y^2} \frac{\partial^2\psi_n}{\partial x^2} - 2 \frac{\partial^2\bar{\psi}}{\partial x\partial y} \frac{\partial^2\psi_n}{\partial x\partial y} \right] \end{aligned} \quad (\text{A6})$$

$$q_n = \frac{g\kappa\pi}{p} \left[ (f + \nabla^2\bar{\psi}) \frac{\partial^2\phi_n}{\partial\pi^2} + \frac{\partial^2\bar{\phi}}{\partial\pi^2} \nabla^2\psi_n + L(\bar{\phi}, \psi_n) + L(\bar{\psi}, \phi_n) \right], \quad (\text{A7})$$

where  $(\bar{\quad}) = (\quad)_0 + \frac{1}{2}(\quad)$ , and

$$L(A, B) = -\frac{\partial^2 A}{\partial x \partial \pi} \frac{\partial^2 B}{\partial x \partial \pi} - \frac{\partial^2 A}{\partial y \partial \pi} \frac{\partial^2 B}{\partial y \partial \pi}, \quad (\text{A8})$$

$$\frac{\partial\phi_n}{\partial\pi} = f \frac{\partial\psi_n}{\partial\pi} = -\theta_n \quad (\text{A9})$$

on the upper and lower boundaries.

In the actual computations, we begin by first mapping the variables onto a 100-km resolution grid by area averaging. The mean values  $q_0$  and  $\theta_0$  are then calculated and (A1)–(A3) solved by an overrelaxation technique to recover  $\phi_0$  and  $\psi_0$ . The iteration was stopped when the difference in the values of  $\phi_0$  and  $\psi_0$  between two successive iterations was less than  $1.0 \text{ m}^2 \text{ s}^{-2}$  and  $1.0 \times 10^4 \text{ m}^2 \text{ s}^{-1}$ , respectively.

For the computation of the EPV anomalies and their inversion, we set  $N = 10$ . For  $n = 1$ , the 1000-mb perturbation  $\theta$  was assigned to  $\theta_1$  and  $q_1 = 0$ . The EPV anomalies at the 900, 800, . . . , 200-mb levels were labeled as  $q_2, q_3, \dots, q_9$ , respectively, and we set  $\theta_n = 0$  for the inversion of these anomalies. For  $n = 10$ , we set  $q_{10} = 0$  and assign the 100-mb perturbation  $\theta$  to  $\theta_{10}$ . We then solved the 20 coupled elliptic equations simultaneously using the overrelaxation technique. The rate of convergence was very slow and it depends on the initial guess field. Using an underrelaxation factor of 0.2, it took about 1000 iterations to obtain an accuracy of  $1.0 \text{ m}^2 \text{ s}^{-2}$  for the geopotential and  $1.0 \times 10^4 \text{ m}^2 \text{ s}^{-1}$  for the streamfunction.

An additional complication arises near the warm frontal zone where the static stability representing the second-order derivative multiplying the horizontal Laplacian of  $\psi_n$  in the second term of (A7) becomes vanishingly small. For smooth inversion, this parameter is set to a constant value of  $1.0 \times 10^2 \text{ K}^2 \text{ J}^{-1} \text{ kg}^{-1}$  at places where it becomes smaller than this value.

#### REFERENCES

- Balashubramanian, G., and M. K. Yau, 1994: Baroclinic instability in a two-layer model with parameterized slantwise convection. *J. Atmos. Sci.*, **51**, 171–190.
- Bennetts, D. A., and B. J. Hoskins, 1979: Conditional symmetric instability—a possible explanation for frontal rainbands. *Quart. J. Roy. Meteor. Soc.*, **115**, 945–962.
- Boyle, J. S., and L. F. Bosart, 1986: Cyclone–anticyclone couplets over North America. Part II: Analysis of a major cyclone event over the eastern United States. *Mon. Wea. Rev.*, **114**, 2432–2465.
- Charney, J. G., 1955: The use of primitive equations of motion in numerical prediction. *Tellus*, **7**, 22–26.
- , and M. E. Stern, 1962: On the stability of internal baroclinic jets in a rotating atmosphere. *J. Atmos. Sci.*, **19**, 159–172.
- Danard, M. B., 1964: On the influence of released latent heat on cyclone development. *J. Appl. Meteor.*, **3**, 27–37.
- Davis, C. A., 1992a: Piecewise potential vorticity inversion. *J. Atmos. Sci.*, **49**, 1397–1411.
- , 1992b: The importance of initial structure and condensational heating in observed extratropical cyclogenesis. *Mon. Wea. Rev.*, **120**, 2409–2428.
- , and K. A. Emanuel, 1991: Potential vorticity diagnostics of cyclogenesis. *Mon. Wea. Rev.*, **119**, 1929–1953.
- , M. T. Stoelinga, and Y. H. Kuo, 1993: The integrated effect of condensation in numerical simulations of extratropical cyclogenesis. *Mon. Wea. Rev.*, **121**, 2309–2330.
- Eliassen, A., and E. Kleinschmidt, 1957: Dynamic meteorology. *Handbuch der Physik*, Vol. 48, Springer-Verlag, 154 pp.
- Ertel, H., 1942: Ein neuer hydrodynamischer wirbelsatz. *Meteor. Z.*, **59**, 271–281.
- Fantini, M., 1990: The effect of heat and moisture fluxes from the ocean on the development of baroclinic waves. *J. Atmos. Sci.*, **47**, 840–855.
- , 1993: A numerical study of two-dimensional moist baroclinic instability. *J. Atmos. Sci.*, **50**, 1199–1210.
- Gyakum, J. R., 1983: On the evolution of the *QE II* storm: Dynamic and thermodynamic structure. *Mon. Wea. Rev.*, **111**, 1156–1173.
- Hedley, M., and M. K. Yau, 1991: Anelastic modeling of explosive cyclogenesis. *J. Atmos. Sci.*, **48**, 711–727.
- Holt, M. W., and A. J. Thorpe, 1991: Localized forcing of slantwise motion at fronts. *Quart. J. Roy. Meteor. Soc.*, **111**, 943–963.
- Hoskins, B. J., and P. Berrisford, 1988: A potential vorticity perspective of the storm of 15–16 October 1987. *Weather*, **43**, 122–129.
- , M. E. McIntyre, and A. W. Robertson, 1985: On the use and significance isentropic potential vorticity maps. *Quart. J. Roy. Meteor. Soc.*, **111**, 877–946.
- Innocentini, V., and E. S. C. Neto, 1992: A numerical study of the role of humidity in the updraft driven by moist slantwise convection. *J. Atmos. Sci.*, **49**, 1092–1106.
- Klemp, J., and R. Wilhelmson, 1978: The simulation of three-dimensional storm dynamics. *J. Atmos. Sci.*, **35**, 1070–1096.
- Kuo, Y. H., and R. J. Reed, 1988: Numerical simulation of an explosively deepening cyclone in the eastern Pacific. *Mon. Wea. Rev.*, **116**, 2081–2105.
- , M. A. Shapiro, and E. G. Donall, 1991a: The interaction between baroclinic and diabatic processes in a numerical simulation of a rapidly intensifying marine cyclone. *Mon. Wea. Rev.*, **119**, 368–384.
- , R. J. Reed, and S. Low-Nam, 1991b: Effects of surface energy fluxes during the early development and rapid intensification stages of seven explosive cyclones in the western Atlantic. *Mon. Wea. Rev.*, **119**, 457–476.
- Liou, C. S., and R. L. Elsberry, 1987: Heat budgets analyses and forecasts of an explosively deepening maritime cyclone. *Mon. Wea. Rev.*, **115**, 1809–1824.
- Manabe, S., 1956: On the contribution of heat released by condensation to the change in pressure pattern. *J. Meteor. Soc. Japan*, **34**, 12–24.
- McWilliams, J. C., 1985: A uniformly valid model spanning the regimes of geostrophic and isotropic stratified turbulence: Balanced turbulence. *J. Atmos. Sci.*, **42**, 1173–1174.
- Neiman, P. J., and M. A. Shapiro, 1993a: The life cycle of an extratropical cyclone. Part I: Frontal evolution and thermodynamic air–sea interaction. *Mon. Wea. Rev.*, **121**, 2153–2176.
- , and —, 1993b: The life cycle of an extratropical cyclone. Part II: Mesoscale structure and diagnostics. *Mon. Wea. Rev.*, **121**, 2177–2199.
- Persson, P. Ola G., and T. T. Warner, 1993: Nonlinear hydrostatic conditional symmetric instability: Implications for numerical weather prediction. *Mon. Wea. Rev.*, **121**, 1821–1833.
- Reed, R. J., M. T. Stoelinga, and Y.-H. Kuo, 1992: A model-aided study of the origin and evolution of the anomalously high po-

- tential vorticity in the inner region of a rapidly deepening marine cyclone. *Mon. Wea. Rev.*, **120**, 893–913.
- Reuter, G. W., and M. K. Yau, 1990: Observations of slantwise convective instability in winter cyclones. *Mon. Wea. Rev.*, **118**, 447–458.
- , and —, 1993: Assessment of slantwise convection in ERICA cyclones. *Mon. Wea. Rev.*, **121**, 3375–3386.
- Robinson, W. A., 1988: Analysis of LIMS data by potential vorticity inversion. *J. Atmos. Sci.*, **45**, 2319–2342.
- Rossby, C. G., 1940: Planetary flow patterns in the atmosphere. *Quart. J. Roy. Meteor. Soc.*, **66** (Suppl.), 68–87.
- Rotunno, R., and K. A. Emanuel, 1987: An air–sea interaction theory for tropical cyclogenesis. Part II: Evolutionary study using a nonhydrostatic axisymmetric numerical model. *J. Atmos. Sci.*, **44**, 542–561.
- Sanders, F., and J. R. Gyakum, 1980: Synoptic–dynamic climatology of the “bomb.” *Mon. Wea. Rev.*, **108**, 1589–1606.
- Smolarkiewicz, P. K., 1983: A simple positive definite advection scheme with small implicit diffusion. *Mon. Wea. Rev.*, **111**, 479–486.
- Takeda, T., 1966: The downdraft in the convective cloud and raindrops: A numerical computation. *J. Meteor. Soc. Japan*, **44**, 1–11.
- Thorpe, A. J., 1985: Diagnosis of balanced vortex structure using potential vorticity. *J. Atmos. Sci.*, **42**, 397–406.
- , and S. A. Clough, 1991: Mesoscale dynamics of cold fronts: Structures described by dropsoundings in FRONTS 87. *Quart. J. Roy. Meteor. Soc.*, **117**, 903–941.
- Tracton, M. S., 1973: The role cumulus convection in the development of extratropical cyclones. *Mon. Wea. Rev.*, **101**, 573–592.
- Whitaker, J. S., L. W. Uccellini, and K. F. Brill, 1988: A model based diagnostic study of the rapid development phase of the Presidents’ Day cyclone. *Mon. Wea. Rev.*, **116**, 2337–2365.